

**EFFECT OF ANNEALING TEMPERATURE ON THE FORMATION OF METHYL-  
AMMONIUM TIN TRI-IODIDE PEROVSKITE THIN FILM**

A thesis presented to the Department of Material Science and Engineering  
African University of Science and Technology, Abuja  
In partial fulfillment of the requirements for the degree of

**MASTER OF SCIENCE**

By

**FRU JUVET NCHE**

Supervised by

Professor Esidor Ntsoenzok



African University of Science and Technology  
[www.aust.edu.ng](http://www.aust.edu.ng)  
P.M.B 681, Garki, Abuja F.C.T  
Nigeria

**July, 2016**

**EFFECT OF ANNEALING TEMPERATURE ON THE FORMATION OF METHYL-AMMONIUM TIN TRI-IODIDE PEROVSKITE THIN FILM**

By

**FRU JUVET NCHE**

A THESIS APPROVED BY THE DEPARTMENT OF MATERIAL SCIENCE AND  
ENGINEERING

**RECOMMENDED:**

---

**Supervisor,** Professor Esidor Ntsoenzok

---

**Co-Supervisor,** Dr. Zebaze Kana

---

Professor Peter Azikiwe Onwuallu  
**Head,** Department of Material Science and Engineering

**APPROVED:**

---

**Chief Academic Officer**

---

**Date**

## ABSTRACT

Organic-inorganic perovskite photovoltaics (PVs) have attracted a lot of attention as high-efficiency thin film PVs which are relatively cheap and easy to fabricate. Lead halide perovskites have shown a rapid rise in power conversion efficiency by 3.8 % in 2009 to 21.02 % in 2016. One major problem is that lead is toxic and poses a serious concern to health and the environment. The most likely substitute for lead is tin. Tin-based perovskite solar cells have shown good semiconducting properties but still have very low efficiencies. The major challenge is the instability of tin in its +2 oxidation state. The photovoltaic performance and life span of these solar cells depend greatly on the film morphology. The morphology depends on the deposition technique and the subsequent treatment employed. In this work, we investigated the effect of post annealing temperature on the formation of methyl ammonium tin tri-iodide ( $\text{CH}_3\text{NH}_3\text{SnI}_3$ ). The  $\text{SnI}_2/\text{CH}_3\text{NH}_3\text{I}$  was formed by sequential thermal evaporation of  $\text{SnI}_2$  followed by evaporation of  $\text{CH}_3\text{NH}_3\text{I}$  on a glass substrate. As-deposited  $\text{SnI}_2/\text{CH}_3\text{NH}_3\text{I}$  films on glass substrate are annealed at different temperatures (80 °C, 90 °C, 100 °C, 110 °C, and 120 °C) in nitrogen atmosphere. Resistivity measurements and X-ray Diffraction (XRD) show that the best annealing temperature range for the formation of  $\text{CH}_3\text{NH}_3\text{SnI}_3$  may be between 80 °C and 100 °C.

## **ACKNOWLEDGMENT**

I wish to render my heartfelt gratitude to my supervisor Prof. Esidor Ntsoenzok for his guidance, time, attention, encouragement and above all material support. He single-handedly purchased and mailed the chemicals for this project. Thanks to his quick intervention, I was able to perform the first experiments on organic-inorganic perovskites at AUST, Abuja.

I also wish to express my sincere appreciation to Dr. Zebaze Kana for his encouragement, time, attention and valuable contributions that enabled me to perform this experiment in Kwara State University Materials Science Laboratory. Immense thanks to Dr. Vitalis Anye for his guidance, support, and encouragement.

I also wish to thank all my colleagues in the class, especially those in the energy group for their support. Sincere thanks also go to all the lab technologies in Kwara State University (KWASU) Materials Science Laboratory for their technical support.

Sincere gratitude goes to the Pan African Materials Institute (PAMI) for their financial support for this project. PAMI paid for my transportation, lodging, feeding, consumables and bench fee at KWASU. I want to use this opportunity to sincerely thank the Nelson Mandela Institution (NMI) for providing me with a full scholarship to study materials science and engineering at AUST, Abuja.

## **DEDICATION**

This thesis is dedicated to my Grandmother Frida Azah of Blessed Memory.

## CONTENTS

ABSTRACT	iii
ACKNOWLEDGMENT	iv
DEDICATION	v
CONTENTS	vi
LIST OF FIGURES	ix
LIST OF TABLES	x
CHAPTER ONE	1
GENERAL INTRODUCTION	1
1.1 Problem Definition	1
1.2 Aim and Objectives	2
1.3 Outline of Thesis	2
CHAPTER TWO	3
FUNDAMENTALS OF PV TECHNOLOGY	3
2.1 Solar Energy and Solar Power	3
2.2 PVs	3
2.3 Evolution of Solar Cells	3
2.3.1 First Generation	3
2.3.2 Second Generation	4
2.3.3 Third Generation	5
2.3.4 Multi-junction Solar Cells (Tandem Junction Solar Cells)	8
2.4 Parameters for Electrical Characterizations of PVs	9
2.4.1 Short-Circuit Current ( $I_{sc}$ )	9
2.4.2 Open Circuit Voltage ( $V_{oc}$ )	10
2.4.3 Fill Factor (FF)	10
2.4.4 Power Conversion Efficiency (PCE or $\eta$ )	11
2.5 PEROVSKITE SOLAR CELLS (Pscs)	12

2.6	Introduction	12
2.7	Previous Works	12
2.8	Architecture of PSCs	14
	Figure 2.6. Perovskite Solar Cell Architectures	14
2.9	The p-i-n Junction in PSCs	15
2.10	Materials	16
2.10.1	Hole Transport Materials (HTM)	16
2.10.2	Electron Transport Materials (ETM)	17
2.10.3	Back Contact Materials	17
2.10.4	Active Layer (Perovskite) Materials	18
2.10.5	Transparent Conducting Oxide (TCO)	19
2.10.6	Substrate Materials	20
2.10.7	Processing Techniques of Perovskite Solar Cells	20
2.10.8	Physical Concepts of PSCs	23
2.10.9	Principle of Light Absorption and Free Charge Generation	24
2.10.10	Stability of PSCs	25
2.10.11	Crystal Structure and Tolerance Factor of PSCs	26
	CHAPTER THREE	28
	EXPERIMENTAL PROCEDURE	28
3.1	Equipment	28
3.2	Chemicals	28
3.3	Fabrication of Perovskite Layer	28
3.3.1	Cleaning of Glass Slides	28
3.3.2	Sequential Thermal Vacuum Deposition of $\text{CH}_3\text{NH}_3\text{SnI}_3$	29
3.3.3	Annealing of $\text{CH}_3\text{NH}_3\text{SnI}_3$	30
3.4	Characterizations of $\text{CH}_3\text{NH}_3\text{SnI}_3$ Perovskite	31
3.4.1	Optical Measurement	31
3.5	Electrical Measurement	31
3.5.1	X-ray Diffraction (XRD)	32
	CHAPTER FOUR	33

RESULTS AND DISCUSSIONS	33
4.1 Variation of Transmittance with Annealing Temperature	33
4.2 Stability of Un-Annealed and Annealed Films in Air	33
4.3 Absorption Coefficient, $\alpha$	34
4.4 Variation Surface Roughness with Annealing Temperature	35
4.5 Resistivity	37
4.6 X-ray Diffraction (XRD)	38
CHAPTER FIVE	41
CONCLUSION AND RECOMMENDATIONS FOR FUTURE WORK	41
REFERENCES	42

## LIST OF FIGURES

Figure 2.1. First Generation Solar Cell [10].....	4
Figure 2.2. p-n heterojunction thin film solar cell of CdTe/CdS [10].....	5
Figure 2.3: Schematic of the structure of the dye sensitized solar cell[13].....	6
Figure 2.4. (a) Planar (Bi-layer) heterojunction organic solar cell and (b) Bulk heterojunction organic solar cell[16].....	7
Figure 2.5: Tandem Junction Solar Cell Architecture (top) and Examples (bottom) [17].....	9
Figure 2.6. Perovskite Solar Cell Architectures.....	14
Figure 2.7: Perovskite Crystal Structure [33].....	19
Figure 2.8: One-Step and Two-Step Coating Procedures to Deposit CH <sub>3</sub> NH <sub>3</sub> PbI <sub>3</sub> Perovskite [48].....	21
Figure 2.9: Dual-source thermal evaporation for deposition of perovskite absorber [42].....	22
Figure 2.10: Vapor-assisted solution process using the MAI organic vapor to react with the PbI <sub>2</sub> [44].....	23
Figure 2.11: Sequential deposition by dipping the PbI <sub>2</sub> in MAI Solution to form MAPbI <sub>3</sub> [44].	24
Figure 2.12. Free charge generation and transport.....	25
Figure 3.1. Ultrasonic Cleaner.....	29
Figure 3.2. Nano 36 Thermal Vacuum Evaporator.....	30
Figure 3.3. Sequential Thermal Evaporation of SnI <sub>2</sub> /CH <sub>3</sub> NH <sub>3</sub> I Thin Film.....	30
Figure 3.4. Annealing of SnI <sub>2</sub> /CH <sub>3</sub> NH <sub>3</sub> I in Vacuum Oven under Nitrogen Environment.....	30
Figure 3.5. AVASPEC Fiber Optic Spectrophotometer.....	31
Figure 3.6. Keithley Source Meter Unit set Up (Left) and X-ray Diffractometer (right).....	32
Figure 4.1. Variation of Transmittance of SnI <sub>2</sub> /CH <sub>3</sub> NH <sub>3</sub> I with Annealing Temperature.....	33
Figure 4.2. Variation of Transmittance of unannealed SnI <sub>2</sub> /CH <sub>3</sub> NH <sub>3</sub> I with time.....	34
Figure 4.3. Variation of Transmittance of SnI <sub>2</sub> /CH <sub>3</sub> NH <sub>3</sub> I Thin Film Annealed at 110 °C with time.....	34
Figure 4.4. Variation of Absorption Coefficient of SnI <sub>2</sub> /CH <sub>3</sub> NH <sub>3</sub> I Thin Film with Annealing Temperature.....	35
Figure 4.5. SPM Images of Surface Layer of Films Annealed at (b) 80 °C (c) 100 °C (d) 120 °C and (a) Un-annealed.....	36
Figure 4.6. Variation of Resistivity with Post Annealing Temperature in Formation of SnI <sub>2</sub> /CH <sub>3</sub> NH <sub>3</sub> I Thin Film.....	38
Figure 4.7. XRD for un-annealed Film.....	39
Figure 4.8. XRD for film annealed at 80 °C.....	39
Figure 4.9. XRD Pattern Derived from Ground Powder of CH <sub>3</sub> NH <sub>3</sub> SnI <sub>3</sub> [2].....	40

## LIST OF TABLES

Table 2.1. Work Functions for Some Metal Contact Materials	18
Table 2.2. Ionic Radii for Some Ionic Species	26
Table 2.3. Tolerance Factors for Organic-Inorganic Perovskites	27
Table 4.1. Roughness of SnI <sub>2</sub> /CH <sub>3</sub> NH <sub>3</sub> I Thin Films Annealed at Different Temperatures	37

# CHAPTER ONE

## GENERAL INTRODUCTION

### 1.1 Problem Definition

The demand for energy is increasing and the danger of global warming due to CO<sub>2</sub> emissions are the tremendous future challenges for mankind. It is well known that the use of conventional energy sources (coal, natural gas, and petroleum) contribute a huge amount of CO<sub>2</sub> to the environment. There is, therefore, growing need for alternative energy sources that are green and sustainable. Solar power is the world's most abundant energy resource [1]. A year's worth of sunlight contains  $1.5 \times 10^{18}$  kW h of energy. Harvesting the solar energy is an essential approach to providing green and sustainable energy. One way of harvesting from the sun is by the use of photovoltaics or solar cells.

The photovoltaic market is dominated by conventional solar cells made of crystalline silicon [2]. Although these solar cells are well established and reasonably efficient, they are relatively expensive to produce for low-income earners. It is still not economically feasible to use crystalline silicon solar cells in many regions because of their high production and installation costs [3]. The scarcity of some of the elements required to make solar grade silicon is another major obstacle that makes silicon solar cells to be non-sustainable. Silicon-based single junction solar cells have in recent decades recorded a slow rise in efficiencies [4]. Hence, new materials and novel solar technologies are being developed in an effort to find cells that are cheaper and more sustainable when compared to silicon solar cells [5].

Alternative “third generation” PVs such as organic photovoltaics (OPVs), dye sensitized solar cells (DSSCs), quantum dot solar cells (QDSCs) and perovskite solar cells, are fabricated through solution based methods. They promise low-cost solar power while allowing the utilization of unconventional substrates. However, the power conversion efficiencies (PCEs) of most of these solar cells still lag significantly behind conventional solar cells. Organic-inorganic halide perovskite solar cells satisfy the need for high efficiencies and allow for low-cost solution based manufacturing. The PV efficiencies of devices fabricated with these materials have increased from 3.8% in 2009 [5] to a certified 21.02% in 2015 [6], making this the fastest-

advancing solar technology to date [7]. Presently, the most efficient perovskite PVs are lead-based. The use of lead poses health and environmental problems. Therefore, there is a need for replacement of lead with less toxic materials like tin, copper, iron, etc. This research intends to investigate the possibility of using tin in place of lead for the fabrication of perovskite PVs.

## 1.2 Aim and Objectives

This thesis explores the effect of post annealing temperature on the structural, composition, optical and electrical properties of  $\text{CH}_3\text{NH}_3\text{SnI}_3$  film formed by thermal vacuum evaporation.

The objectives of this research are to:

- Determine the conditions for thermal vacuum deposition of  $\text{SnI}_2$  on a glass substrate that is kept at room temperature using a thermal evaporator
- Determine the conditions for thermal vacuum deposition of  $\text{CH}_3\text{NH}_3\text{I}$
- Form a thin film  $\text{CH}_3\text{NH}_3\text{I} / \text{SnI}_2$  using sequential vacuum deposition on glass substrate that is kept at room temperature using a thermal evaporator
- Determine the change in the optical properties of as-deposited  $\text{CH}_3\text{NH}_3\text{I} / \text{SnI}_2$  with time
- Anneal the  $\text{CH}_3\text{NH}_3\text{I} / \text{SnI}_2 / \text{glass}$  in a vacuum oven at different temperatures
- Measure sheet resistance of the thin films using the four point probe
- Determination of phases present using X-ray Diffraction (XRD)

## 1.3 Outline of Thesis

Following the introduction in chapter one, is a detailed background and literature review presented in chapter two including a detailed review of perovskite solar cells is presented. This is followed by chapter three in which the experimental procedures are described. The results obtained from the studies of composition, –electrical and optical properties are presented in chapter four before summarizing the important conclusions and presenting suggestions for future work in chapter five.

## CHAPTER TWO

### FUNDAMENTALS OF PV TECHNOLOGY

#### 2.1 Solar Energy and Solar Power

The sun is considered to produce a constant amount of energy. Solar energy is radiant light and heat from the sun. The sun emits  $3.8 \times 10^{26}$  watts of power, an amount of energy each second equal to  $3.8 \times 10^{26}$  joules [8]. At the surface of the sun, the intensity of solar radiation is about  $6.33 \times 10^7 \text{ W/m}^2$  [9]. The atmosphere scatters, absorbs and reflects some of the sun's energy that is incident on the earth's surface. The quantity of energy reflected, scattered and absorbed depends on the quantity of atmosphere that the incident radiation goes through. It also depends on the amount of dust particles and water vapor present in the atmosphere [21]. The solar constant is the average intensity of radiation falling on an imaginary surface and perpendicular to the sun's rays at the edge of the earth's atmosphere. A yearly average value of the solar constant is taken to be  $1367 \text{ W/m}^2$  [9]. This energy is harnessed using a range of ever-evolving technologies such as PVs, solar thermal, solar architecture and artificial photosynthesis. Solar panels (array of PVs) are calibrated assuming that this is  $1000 \text{ W/m}^2$  available [9].

#### 2.2 PVs

Solar cell or PV is defined as a device whose electrical characteristics, such as current, voltage, or resistance, vary when exposed to light. It is an electrical device that converts the energy of light directly into electricity by the photovoltaic effect.

#### 2.3 Evolution of Solar Cells

##### 2.3.1 First Generation

First generation solar cells have large p-n junctions produced on wafers made of one kind of material, **Figure 2.1**. Such a junction is called a homojunction. Common materials for wafers include crystalline silicon (c-Si), amorphous silicon (a-Si) and gallium arsenide (GaAs) [10]. It is the oldest and most widely used technology because of its high-efficiency [11]. According to Mohammad Taw heed Kibria et al. in 2014, the first generation laboratory based efficiency was 24.7 % and the module-based efficiency was 22.7 %. There are generally two types of first generation solar cells; single crystal solar cell and multi-crystal solar cell. In a single or mono

crystal solar cell, the whole wafer is only one grain. Multi-crystal solar cells have wafers with many grains with distinct grain boundaries. Mono crystal solar cells have a higher efficiency than multi-crystal solar cells, but the latter is easier and cheaper to produce. Each wafer can supply 2-3 watt power. Modules, which consist of many solar wafers, are used to increase power supply. This type of solar cells dominate the market; 90 % of the market [10], and are mainly those seen on rooftops. The advantages of this solar cell technology lie in their good performance, as well as their high stability. The main disadvantage of this technology is that silicon wafers are quite expensive.

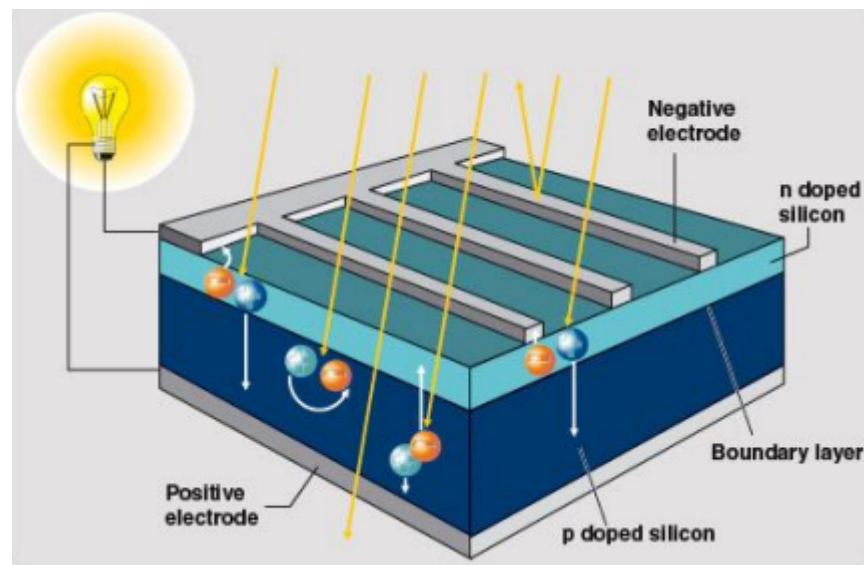


**Figure 2.1.** First Generation Solar Cell [10]

### 2.3.2 Second Generation

Second generation solar cells make use of thin film technology. They contain p-n heterojunctions with thin films. They include amorphous silicon-based thin film solar cells, cadmium telluride/cadmium sulfide (CdTe/CdS) solar cells, copper indium gallium selenide (CIGS) solar cells, and other examples. The cells are built up in the following order from bottom to top: metal base contact, an n-type layer, an intrinsic layer, a p-type layer, a transparent contact layer and glass substrate. The thin films can also be grown on flexible substrates thus are much more applicable in windows of houses and cars. They can be grown on large areas up to 6 m<sup>2</sup> whereas wafer based solar cells can only be produced on wafer dimensions. This technology consumes less material and uses low-cost manufacturing processes. Thus, panels are produced

and sold at a lower cost than first generation panels. Thin film solar cells have lower efficiency than wafer based solar cells and consume a larger area per watt production. This generation of solar cells has a lab-based efficiency of 18.4 % and a module-based efficiency of 13.4 % [11]. The market share of all thin film technologies amounted to about 9 % of the total annual production in 2014 [12].

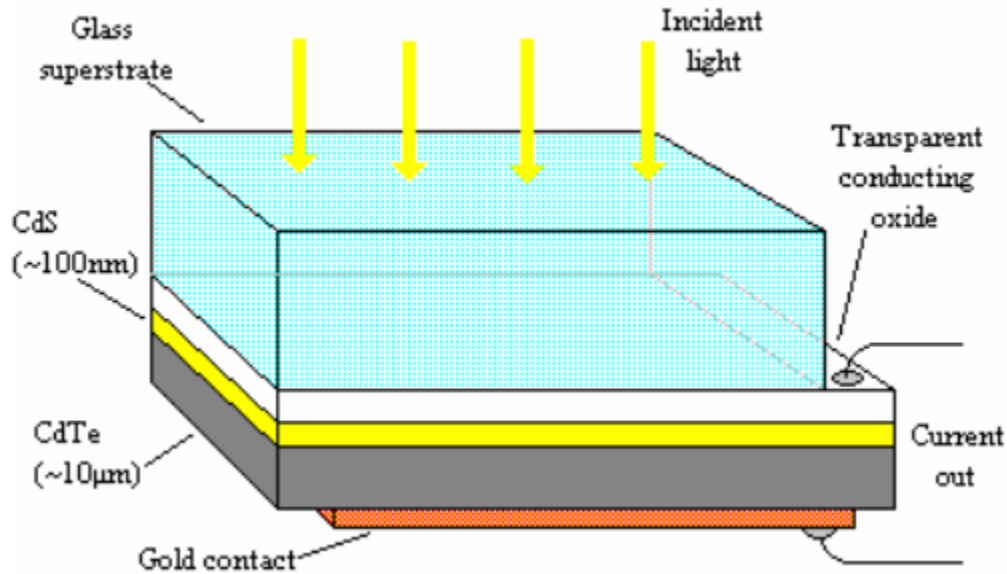


**Figure 2.2.** P-n heterojunction thin film solar cell of CdTe/CdS [10]

In **Figure 2.2**, CdS is n-doped, has a band gap of 2.5 eV and is the window layer. CdTe is p-doped, has a band gap of 1.5 eV and is the active layer. The concentration of dopants on the p-side is far less than the concentration dopants on the n-side ( $p \ll n$ ).

### 2.3.3 Third Generation

Third generation cells have no p-n junction. They are based on Donor-Acceptor interfaces. Examples include nanocrystal (quantum dot) based solar cells, polymer based solar cells, dye sensitized solar cells, concentrated solar cells and the fast emerging perovskite solar cells. These are novel technologies which are promising but have not yet been commercially proven and the market share is still 0 % [11]. They have very low efficiencies; less than 10 % [10] and also very low-cost.

#### *Nanocrystal Based Solar Cells*

Nanocrystal based solar cells are built up of a semiconductor (silicon) coated with a very thin layer of quantum dots. Quantum dots are crystals of a few nanometers in diameter and are used as the absorbing photovoltaic material. These crystals are mixed into a solution and placed on silicon which is being rotated at a very fast rate. The crystals spread on the silicon with the help of the centrifugal force. Quantum dots have an advantage over bulk semiconductor materials in that one can tune the bandgap by a simple change of particle size without changing the underlying materials or processing technique. The use of quantum dots improves efficiency in that more than one electron-hole pairs are generated when a quantum dot absorbs a photon, unlike bulk semiconductor materials where a single photon emits only one electron hole-pair.

### ***Dye Sensitized Solar Cells***

Dye sensitized solar cells are based on dye molecules (typically ruthenium polypyridine) between electrodes [11]. They are composed of four main parts; the transparent conducting and counter conducting electrodes, the nanostructured wide bandgap semiconducting layer, the dye molecules (sensitizer), and the electrolyte [13]. The dye molecules inject electrons into the titanium dioxide semiconducting layer (acceptor) upon photoexcitation. The semiconductor transports the electrons away and the electrolyte (donor) closes the circuit so that the electrons can return to the dye.

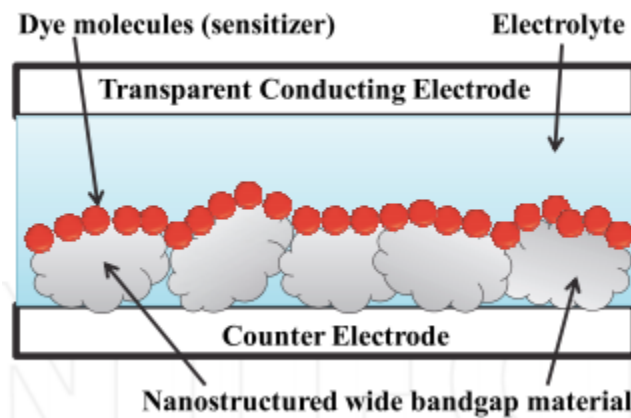


**Figure 2.3:** Schematic of the structure of the dye sensitized solar cell[13]

### ***Organic Solar Cells***

Organic solar cells (**Figure 2.4**) are based on conductive organic polymers and small organic molecules, for light absorption and charge transport. In the planar heterojunction architecture, the light absorbing layer is composed of a p-type (electron donor, D) and an n-type (electron, A) material. This light absorbing layer is sandwiched between a transparent anode (example Indium Tin Oxide (ITO)) with high work function and a metallic cathode (example Al, Mg or Ca with low work function). The absorption of a photon by the p-type material leads to the generation of Frankel excitons which diffuse to the D/A interface. At the interface, the effective electric field is strong enough to break up the excitons into free electrons and free holes by causing the electrons to fall from the lowest unoccupied molecular orbital (LUMO) of the absorber material to the LUMO of the acceptor molecule (with higher electron affinity). The holes are then transported to the anode and the electrons to the cathode to supply direct current to the consumer load. Some examples of electron-donating materials include; P3HT, PBTT, and MDMO-PPV. Electron-accepting materials are mostly derivatives of fullerene such as PC<sub>60</sub>BM, PC<sub>61</sub>BM, PC<sub>70</sub>BM and PDI [14]. The diffusion length of excitons in organic electronic materials is relatively short and is typically on the order of 10 nm. This is due to the fact that organic semiconductors have low dielectric constants when compared to inorganic semiconductors. In order to achieve efficient electron transfer between donor and acceptor, it is necessary that the two materials are within the range 10 nm [27]. Organic materials, however, need a minimum thickness of 100 nm in order to maximize light absorption. This problem is solved by optimizing the interface between the acceptor and donor. This is achieved by making use of dispersed or bulk heterojunction morphology during fabrication [15]. In this bulk heterojunction architecture, an interpenetrating network of the donor and acceptor materials is created with high interface surface area while still providing channels for charge transport to electrodes.



(a) Planer heterojunction organic solar cell

(b) Bulk heterojunction organic solar cell

**Figure 2.4.** (a) Planar (Bi-layer) heterojunction organic solar cell and (b) Bulk heterojunction organic solar cell[16]

Some advantages of organic solar cells include high optical absorption coefficients that permit the use of very thin films, low weight and flexible thus compactible with plastic substrates, inexpensive to fabricate and use of earth-abundant and non-toxic materials. The efficiency is too low with a record value of 5 %. The low efficiencies of organic solar cells are related to the small exciton diffusion lengths and low carrier mobility.

### 2.3.4 Multi-junction Solar Cells (Tandem Junction Solar Cells)

There are two configurations of multi-junction solar cells; the parallel configuration and the series or tandem configuration. The series or tandem junction solar cell (**Figure 2.5**) is the most frequently used. It consists of different p-n junction solar cells placed one on the other. The cell with the largest band gap ( $E_{1g}$ ) placed at the top and the cell with the least band gap ( $E_{3g}$ ) at the bottom. This enables the utilization of a greater part of the electromagnetic spectrum. They are fabricated from monocrystalline Si/microcrystalline Si and organic or inorganic (example, group's III-V) compounds. The crystal structure/lattice constants of all layers must be similar. This is to enhance performance by avoiding defects or dislocations at interfaces which are preferred recombination sites. The output current is limited to the individual currents produced at the individual junctions but the voltage produced is added [17]. The power conversion efficiency increases with a number of cells and can be calculated using the Shockley-Queisser theory.

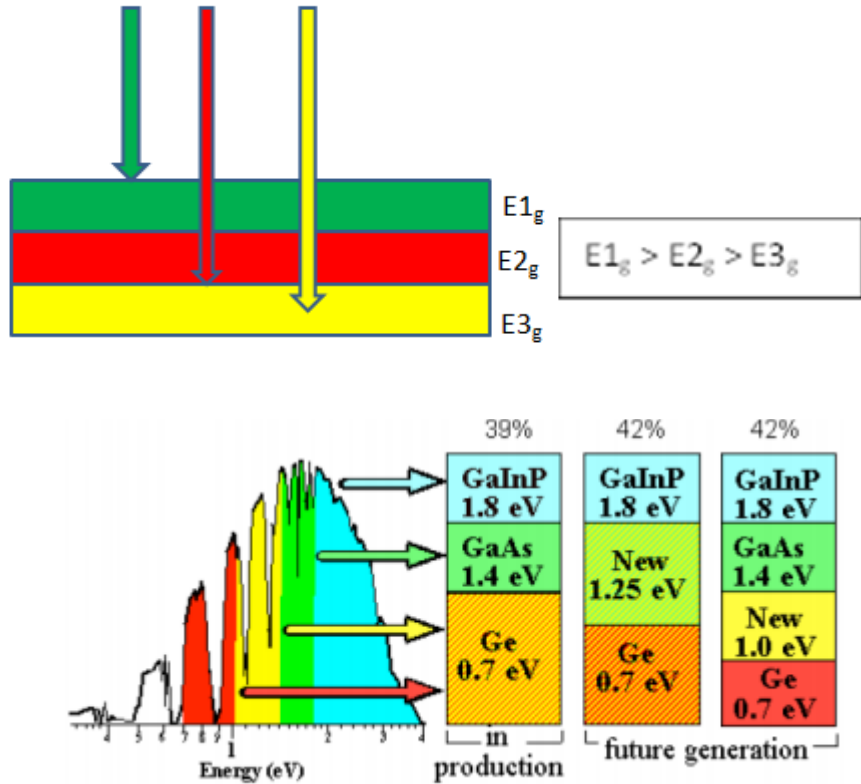


**Figure 2.5:** Tandem Junction Solar Cell Architecture (top) and Examples (bottom) [17]

## 2.4 Parameters for Electrical Characterizations of PVs

### 2.4.1 Short-Circuit Current ( $I_{sc}$ )

$I_{sc}$  is the largest current which may be drawn from a solar cell. It is the current through a solar cell when the voltage across the cell is zero and is due to the generation and collection of photo-generated carriers. Excessive series resistance reduces the short-circuit current. For a solar cell with moderate resistive losses, the short-circuit current is equal to the photo-generated current. The series resistance in solar cells is the resistance due to the movement of current between the emitter and the base of the solar cell, the resistance at the semiconductor/metal contacts and the resistance of the metal contacts. The short-circuit current also depends on the optical losses of the solar cell, the power of the incident light source, the collection probability and the surface area of the solar cell. Optical losses refer to light that is reflected from the front contact and/or light that is not absorbed by the solar cell. Such losses reduce the short-circuit current and hence reduce the power from a solar cell. The dependence of  $I_{sc}$  on surface area is removed by using the short-circuit current density ( $J_{sc}$  in  $\text{mA}/\text{cm}^2$ ). The collection probability depends on the

surface recombination. High surface recombination tends to reduce the short-circuit current. Surface recombination can be reduced by passivating the surface with silicon dioxide due to low defect state at the interface or by using dielectric layers such as silicon nitride. Heavy doping under metal contacts also reduces the amount of surface recombination by keeping minority carriers away from the high metal contacts. In a cell with perfectly passivated surface and uniform generation, the equation for the short-circuit current density can be approximated as in equation 2-2 [18]:

$$J_{SC} = qG(L_n + L_p) \dots\dots\dots\text{Equation 2-1}$$

Where G is the generation rate and  $L_n$  and  $L_p$  are the electron and hole diffusion lengths respectively. This shows that the short-circuit current density depends strongly on the generation rate and on diffusion lengths of charge carriers. For an ideal solar cell  $J_{sc} = 35\text{mA/cm}^2$  [18].

#### 2.4.2 Open Circuit Voltage ( $V_{oc}$ )

The open circuit voltage is the maximum voltage available from a solar cell and occurs when the net current through the device is zero ( $I = 0$  mA). At  $V_{oc}$  the solar delivers maximum voltage but the output power is zero since  $I = 0$  mA. An equation for  $V_{oc}$  is found by setting the net current equal to zero in the solar cell equation to give equation 2-3 [18]:

$$V_{oc} = \frac{nkT}{q} \ln\left(\frac{I_L}{I_o} + 1\right) \dots\dots\dots\text{Equation 2-2}$$

Where K is the Boltzmann’s constant, T is the absolute temperature, n is the ideality factor, q is the absolute value of the electron charge,  $I_L$  is the photo-generated current and  $I_o$  is the reverse saturation current or “dark saturation current”. The main effect on  $V_{oc}$  is  $I_o$  since  $I_L$  generally has small variations.  $I_o$  depends on the recombination in the device, a device with larger recombination will have a large  $I_o$ . Thus,  $V_{oc}$  is a measure of the amount of recombination in the device. Better quality devices have higher open circuit voltages. For example, high quality single crystalline silicon solar cells have an open circuit voltage of about 730 mV under one sun and AM1.5 conditions [18] while commercial devices on multi-crystalline silicon typical open circuit voltages of about 600 mV [18].

### 2.4.3 Fill Factor (FF)

The FF is the ratio of the maximum power from a solar cell to the product of Voc and Isc. The FF measures the “squareness” of the solar cell characteristic. It can be determined from current-voltage (I-V) characteristic by evaluating the area of the largest rectangle which will fit in the I-V characteristic. Mathematically, it can be calculated as equation 2-3.

$$FF = \frac{V_m I_m}{I_{sc} V_{oc}} \dots\dots\dots \text{Equation 2-3}$$

Where  $V_m$  and  $I_m$  are the maximum output voltage and current respectively.

FF determines the quality of a solar cell. Cells with high FF have a low equivalent series resistance and a high equivalent shunt resistance. Therefore a small amount of the current produced by the cell is dissipated as internal losses. The bulk resistance at the junction, the contact resistance between the junction and electrodes and the resistance of the electrodes all contribute to the bulk resistance. Recombination in non-ideal solar cells also results in a decrease in FF.

### 2.4.4 Power Conversion Efficiency (PCE or $\eta$ )

It is defined as the ratio of power output ( $P_{out}$ ) from a solar cell to the input power ( $P_{in}$ ) from the sun. PCE is the parameter that is most commonly used to compare the performance of one solar cell to another and it depends on the spectrum and intensity of sunlight and the temperature of the solar cell. Earth based solar cells are measured under AM1.5 and at a temperature of 300K. The irradiance of AM1.5 spectrum corresponds to an input intensity of 1000 W/m<sup>2</sup>. Mathematically, it can be calculated from equation 2-4.

$$\eta = \frac{P_{max}}{P_{in}} = \frac{V_{oc} I_{sc} FF}{P_{in}} \dots\dots\dots \text{Equation 2-4}$$

The PCE of a practical solar cell is far less than 100% for the following reasons:

- **Loss due to non-absorption of long wavelengths.** Long wavelengths may lead to photon

$\frac{hc}{\lambda}$  energy (  $\lambda$  ) that is smaller than the bandgap energy resulting in non-absorption.

- **Loss due to thermalization of the excess energy of photons.** For photovoltaic applications, photon energy greater than the band gap energy is wasted as heat electrons quickly fall back to the conduction band edge.
- **Loss due to total reflection.** Reflection loss occurs mostly from the top surface of the solar cell which receives light. It affects the  $I_{sc}$  of the solar cell since it reduces the absorbed carriers. Reflection from the top surface can be reduced using antireflection coatings (example  $SiO_2$  and  $Si_3N_3$ ) and texturing (with  $H_2SO_4$  or  $HNO_3$  in  $H_2O_2$ ).
- Loss due to incomplete absorption due to the finite thickness of the active layer.
- Voltage drop due to leakage current which is characterized by the shunt resistance.
- Loss due to recombination.
- **Loss due to metal electrode coverage, shading losses.** The area that is covered by the electrode effectively decreases the active area of the solar cell through which the light enters the solar cell. The coverage factor is given by equation 2-5.

$$\frac{A_f}{A_{tot}} \dots\dots\dots \text{Equation 2-5}$$

It determines the shading losses.  $A_{tot}$  is the total area and  $A_f$  is the cell area that is not covered by the electrode. This can be reduced by placing both of the electrodes at the back contact.

- Loss due to voltage factor. The voltage factor ( $\frac{qV_{oc}}{E_g}$ ) describes the absorbed photon energy losses below the band gap.
- Loss due to fill factor.

## 2.5 PEROVSKITE SOLAR CELLS (PSCs)

### 2.6 Introduction

PSC is a third generation PV technology that can be fabricated on glass, metal, polymers, and cement. It is the fastest growing solar cell technology. It makes use of organic-inorganic perovskite material for the active layer for light absorption and charges transport. The following discussion includes the various architectures, materials, and roles of different sections, processing techniques and working principles of the device.

## 2.7 Previous Works

The first report of a solar cell incorporating perovskite light absorber with an efficiency of 3.8% was in 2009 by Miyasaka et al.[19]. They demonstrated the first perovskite sensitized solar cells using  $\text{CH}_3\text{NH}_3\text{PbI}_3$  and  $\text{CH}_3\text{NH}_3\text{PbBr}_3$  as light absorbers on  $\text{TiO}_2$  mesoporous layers with halide electrolytes. In 2011, improvements were made in such liquid electrolyte solar cells by N. G. Park et al.[20], through a careful optimization of the mesoporous layer thickness, perovskite concentration, and surface treatment. They modified the surface of  $\text{TiO}_2$  with  $\text{Pb}(\text{NO}_3)_2$  prior to deposition of perovskites and obtained an efficiency of 6.54% [20]. In spite of the achievements in efficiency, these configurations of solar cells were very unstable because of the dissolution of the perovskite in a liquid electrolyte. A significant improvement in both efficiency and stability was achieved in 2012 through utilization of a solid-state hole transporter 2,2',7,7'-tetrakis( N, N-p-dimethoxy-phenyl amino )- 9, 90-spirobifluorene(spiro-OMeTAD) with  $\text{CH}_3\text{NH}_3\text{PbI}_3$  and  $\text{CH}_3\text{NH}_3\text{PbI}_{3-x}\text{Cl}_x$  light absorbers. N. G. Park, M. Gratzel et al.[21], reported a PCE of 9.7% for  $\text{CH}_3\text{NH}_3\text{PbI}_3$  on 0.6  $\mu\text{m}$   $\text{TiO}_2$  layers. James M. Ball et al.[22] reduced the temperature required to process the bulk absorber layer in  $\text{CH}_3\text{NH}_3\text{PbI}_{3-x}\text{Cl}_x$  perovskite solar cells from 500°C to < 150 °C and achieved a power conversion efficiency of 12.3%. Silvia et al. 2013[23] showed that including  $\text{Cl}^-$  in iodide based perovskites is possible for low concentrations and this drastically improved the charge transport within the perovskite layer.

Several authors have demonstrated the use of nanocomposites in perovskite solar cells. A highly stable hole collection layer of carbon nanotube/polymer composites was demonstrated by Hao Li in 2013 [24]. They identified thermal stability as a fundamental problem of perovskite PVs and demonstrated an excellent approach to mitigate thermal degradation by replacing the organic hole transport material (HTM) with polymer-functionalized single-walled carbon nanotubes (SWNTs) that are embedded in an insulating polymer matrix. Strong retardation in thermal degradation was observed and resistance to water ingress was remarkably enhanced as compared to cells employing state-of-the-art organic hole-transporting materials. In 2016, Jiaying Song et al.[25], developed a low-temperature-processed  $\text{ZnO-SnO}_2$  nanocomposite for efficient planar perovskite PVs. These are important developments for achieving long-term stability and high-efficiency perovskite PVs.

Post annealing conditions of processed organic-inorganic perovskite materials have been shown to affect the formation, morphology, performance, composition, and stability. A. Dualeh et al. in 2014 investigated the effect of annealing temperature used in the conversion process to form perovskite material from the deposited precursor solution[26]. They demonstrated that a minimum temperature of 80 °C is required to form the CH<sub>3</sub>NH<sub>3</sub>PbI<sub>3</sub> perovskite. Also, highest performance was achieved for devices fabricated between 80 °C and 100 °C. Chen et al. in 2015, studied annealing effects on CH<sub>3</sub>NH<sub>3</sub>PbI<sub>3</sub> perovskite film for solar cell applications and reported that an optimal annealing temperature of 100 °C would significantly extend the exciton lifetime and yield a higher open circuit voltage [27]. The perovskite films showed different morphologies at different annealing temperatures and CH<sub>3</sub>NH<sub>3</sub>PbI<sub>3</sub> decomposed at 120 °C with PbI<sub>2</sub> phase formed.

The use of lead in organic-inorganic solar cells poses health and environmental problems. Feng Hao et al. 2014[28], reported a lead-free solution processed solid-state photovoltaic device based on methyl ammonium tin tri-iodide perovskite as a light harvester. The device showed a PCE of 5.73 % and an optical absorption onset of 950 nm. Snaith et al. fabricated lead-free organic-inorganic tin halide perovskites for PV applications in 2014. They used the solution processed method and realized a PCE of 6 %[2]. The cells produced were very unstable with the Sn<sup>+2</sup> oxidizing rapidly to Sn<sup>+4</sup>. Kumar et al. [29], compared the use of CsSnI<sub>3</sub> and CsSnI<sub>3</sub> with added SnF<sub>2</sub> as light absorbers in perovskite solar cells in 2014. They observed that pristine CsSnI<sub>3</sub> as light absorber does not result in a functional photovoltaic device while compositions with added SnF<sub>2</sub> display photovoltaic effect with higher photocurrents > 22 mA cm<sup>2</sup> and an optimum PCE of 2.02 % at 20 wt. % SnF<sub>2</sub>. Unfortunately the Voc and fill factor (FF) were limited to 240 mV and 0.34 respectively. K.P. Marshall et al. 2015[30], reported an effective strategy for simultaneously improving both the efficiency and stability of these devices when exposed to air based on the use of an excess of SnI<sub>2</sub> during CsSnI<sub>3</sub> synthesis from CsI and SnI<sub>2</sub>.

## 2.8 Architecture of PSCs

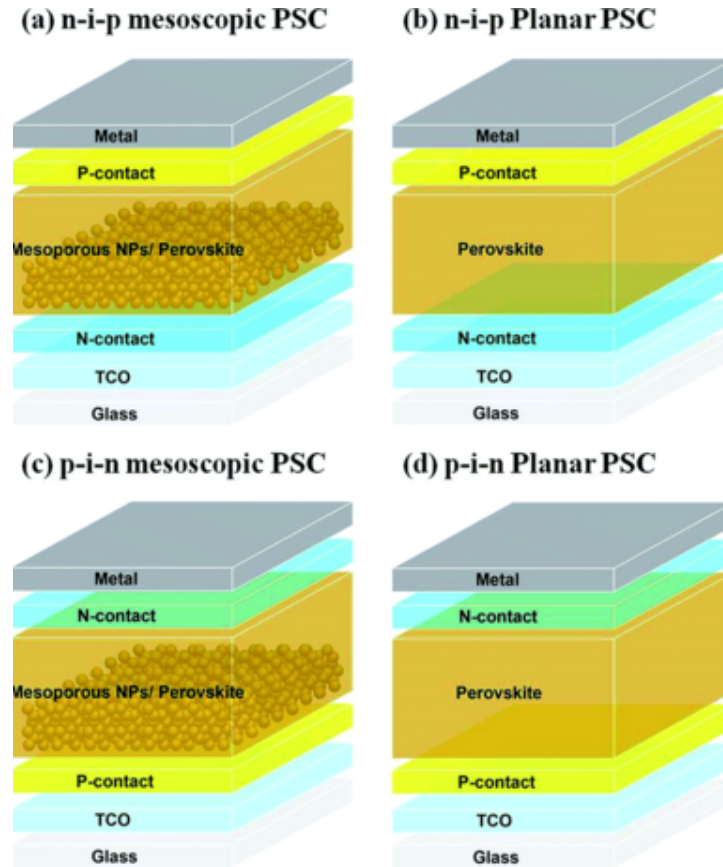


**Figure 2.6.** Perovskite Solar Cell Architectures

A range of device architectures or geometries yielding high efficiencies have been reported [31]. These geometries are the regular (n-i-p) and irregular (p-i-n), each with planar or mesoporous structure. The mesoscopic nanostructured device has a mesoporous oxide layer or scaffold layer for mechanical support.

For regular mesoporous geometry, commonly used n-type semiconducting oxide for the mesoscopic layer is  $\text{TiO}_2$  [31].  $\text{TiO}_2$  has a wide bandgap, non-toxic, cheap, biocompatible and abundant. When used, it provides mechanical support and also assists in electron transport. The use of  $\text{Al}_2\text{O}_3$  in the mesoscopic layer has also been reported [32], but unlike  $\text{TiO}_2$ , this material provides only mechanical support since it is insulating. Fluorine Doped Tin Oxide (FTO) and Indium Tin Oxide (ITO) coated on glass have been used substrates. Glass/FTO/cp- $\text{TiO}_2$ /mp- $\text{TiO}_2$ /perovskite/spiro-OMeTAD/Au and Glass/FTO/cp- $\text{TiO}_2$ /mp- $\text{Al}_2\text{O}_3$ /perovskite/spiro-OMeTAD/Au are some examples of regular mesoscopic architecture [31]. For regular planar

geometry, the perovskite is deposited directly on the compact TiO<sub>2</sub> layer. Examples include: Glass/ FTO/c-TiO<sub>2</sub>/vapor-deposited MAPbI<sub>3-x</sub>Cl<sub>x</sub>/spiro-OMeTAD/Au with PCE of 15.4 % and Glass/ITO/c-ZnO / MAPbI<sub>3</sub> / spiro-OMeTAD / Ag with PCE of 15.7% [31]

## **2.9 The p-i-n Junction in PSCs**

Planar heterojunction perovskite solar cells operate like other p-i-n junction devices. They have a wide intrinsic semiconductor perovskite region, i, between a p-type semiconductor (HTL) and an n-type semiconductor region (ETL). In other words, the perovskite is situated in a built-in electric field. Photovoltaic action in perovskite solar cells heavily depends on these HTL and ETL interfaces. It has been reported that the built-in field resulting from the interfaces can affect bulk dissociation and causes the photo-generated free charge carriers to drift to the respective electrodes where they are extracted [33].

## 2.10 Materials

### 2.10.1 Hole Transport Materials (HTM)

It is well known that organic-inorganic perovskites can serve as light absorption materials and charge transport materials in perovskite solar cells, however, it has been reported that a hole-conductor free mesoscopic  $\text{CH}_3\text{NH}_3\text{PbI}_3/\text{TiO}_2$  heterojunction PV has a PCE of 5.5 %. This value is very low when compared to cells with HTMs [34]. This means that HTMs play a very vital role in improving the performance of perovskite solar cells. They assist in the dissociation of excitons and transport holes to the back electrode when the excitons are dissociated into electrons and holes. They must have valance band edge lying above that of the perovskite and conduction edge above that of the conduction band edge of the perovskite. In this way, it will be able to attract holes and reject electrons. Also, it must be highly conductive to holes.

Another role of HTM is to reduce recombination and increase absorption[35]. So far most of the record-holding perovskite solar cells use spiro-OMeTAD as HTM [34]. HTMs need to be highly conductive in order to reduce the series resistance, however, even the widely used HTMs, for example, spiro-OMeTAD, are less conductive than perovskite materials [34]. Doping improves the FF by enhancing the conductivity of the HTM and reducing the series resistance [35]. Periotic ionic liquid has been used as p-dopant to HTMs [35].

HTMs can be organic or inorganic. Some reported organic HTMs include; spiro-OMeTAD, P3HT, DEH and PDOT: PSS. In terms of performance, Spiro-OMeTAD is the best organic HTM so far but has the following weaknesses. It is commercially expensive and shows pin holes when solution processed. Zafar Hawash et al.[36], discovered the presence of pinholes in solution processed Spiro-OMeTAD layer and also found out that spiro-OMeTAD deposited by vacuum evaporation was pin hole free. Pin hole free cells showed long-term stability. They, therefore, concluded that the pin holes were responsible for the rapid degradation of the cells when exposed to air. Some reported inorganic HTMs include CuI, NiO,  $\text{V}_2\text{O}_5$ ,  $\text{CsSnI}_3$  and copper thiocyanate. They are less expensive than organic HTMs. CuI show very low efficiencies when used but copper thiocyanate is a more efficient HTM for PSCs. Qin et al. incorporated copper thiocyanate with  $\text{CH}_3\text{NH}_3\text{PbI}_3$  as HTM and the device showed PCE of 12.4% [38].

### **2.10.2 Electron Transport Materials (ETM)**

The role of electron transport materials is to assist in electron transport and also to block the hole diffusion. In the absence of electron transport materials, the electron-hole pairs can hardly dissociate and recombination prevails. The ETM must have a conduction band edge or LUMO edge lying below the conduction band edge or LUMO level of the perovskite and the valence band edge lying under the valence band edge of the perovskite. In this way, it attracts the electrons and rejects the holes. It must also have high electron mobility for conducting the electrons to the cathode. Compacted  $\text{TiO}_2$  is commonly used in almost all structures and it effectively blocks the hole transport to the cathode. In mesoscopic structures, porous  $\text{TiO}_2$  materials, such as crystals, nanofibers, and nanotubes are deposited on the compact layer. Other reported ETMs include ZnO,  $\text{TiO}_2$ -graphene composites, and fullerene (PCBM).  $\text{TiO}_2$  has achieved the best device performance in perovskite solar cells thus far.

### **2.10.3 Back Contact Materials**

Metal contacts (electrodes) are needed in solar cells to collect charge carriers and deliver them to the load where power is required. The interface between the semiconductor and the metal must be properly engineered to ensure effective collection and minimal recombination. For perovskite solar cells, this interface can be an inorganic semiconductor/metal or organic semiconductor/metal interface depending on the structure of the solar cell.

Generally, an inorganic semiconductor/metal interface can be ohmic or rectifying, but ohmic contact is more important in conventional solar cells. A potential barrier is formed in both rectifying and ohmic contacts, but in presence of the barrier in ohmic contacts do not render any opposition to the flow of carriers in both directions. For inorganic semiconductors (especially Si), ohmic contact can be achieved by heavily doping the entire semiconductor material or by a gradual doping profile beneath the contact area. Heavy doping causes the space charge region to narrow and allows charge to tunnel to the semiconductor material. For an ohmic contact between a metal and a  $n^+$  type semiconductor, the work function of the metal has to be less than the electron affinity of the  $n^+$  material. On the contrary, for a  $p^+$  type material, the work function of the metal has to be more than the electron affinity of the semiconductor.

The technique of enhancing charge injection by means of heavily local doping of the semiconductor to provide tunneling contact is not always feasible for organic semiconductors. This is because doping in organic semiconductors is an interstitial process unlike for inorganic where doping is substitutional. Also, weak intermolecular interaction in the solid-state of the organic semiconductor introduces a further challenge for achieving tunneling or ohmic contacts. Therefore, good ohmic contact inorganic semiconductor is achieved by proper alignment of the Fermi level of the electrode and the HOMO/LUMO energy levels of the organic material. Proper alignment can be realized by selection of the right electrode metal based on its work function. **Table 2.1**, gives the work functions for different metals that are mostly used as electrode materials [39]. Most high-performance perovskite solar cells with spiro-OMeTAD as HTM have made use of Au and Ag as back electrode materials [31]. Al, Au, Ca/Au have also been reported as back contact materials on PCBM [31]. Al, Ag, and Au have been reported as back contact materials on PCBM/BCP composite layer [40]. Carbon has also been reported as back contact material on NiO [40].

**Table 2.1.** Work Functions for Some Metal Contact Materials

S/N	Material	Work function / eV
1	Al	4.30
2	Cu	4.45
3	Ag	4.35
5	Au	4.85
6	Ni	4.50
7	Cr	4.52
8	Si(n <sup>+</sup> )	4.00

#### 2.10.4 Active Layer (Perovskite) Materials

Organic-inorganic semiconducting perovskites have previously been used in nanostructured solar cells as sensitizers (absorbers), hole transporter, a combined sensitizer and hole transporter and a combined absorber and electron transporter [41]. However, in most p-i-n and n-i-p architectures, these materials play the role of light absorber or sensitizer [31][40]. The generic chemical formula for organic-inorganic halide perovskites is ABX<sub>3</sub>, where the A cations are organic (typically CH<sub>3</sub> NH<sub>3</sub><sup>+</sup>, C<sub>2</sub> H<sub>5</sub> NH<sub>3</sub><sup>+</sup>, HC(NH<sub>2</sub>)<sub>2</sub><sup>+</sup>), the metal cations (B) are typically divalent metal

ions such as  $\text{Pb}^{2+}$ ,  $\text{Sn}^{2+}$ ,  $\text{Eu}^{2+}$ ,  $\text{Cu}^{2+}$  etc., while the X anions are halides ( $\text{Cl}$ ,  $\text{Br}$ ,  $\text{I}^-$ ) [42]. The perovskite crystal structural arrangement is shown in **Figure 2.7**.

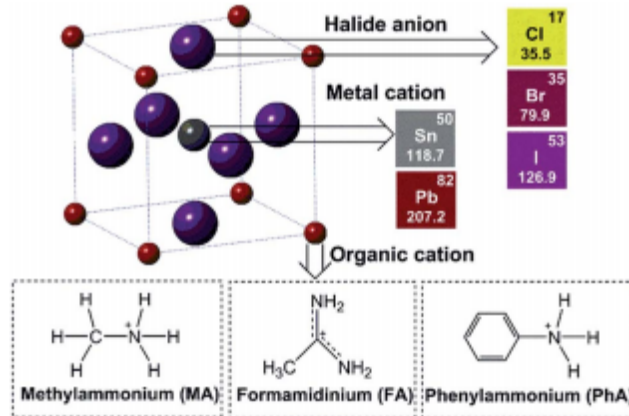


**Figure 2.7:** Perovskite Crystal Structure [33]

Perovskite materials have high absorption coefficients up to  $1.5 \times 10^4 \text{ cm}^{-1}$  at 550 nm for hybrid lead iodide solar[43]. Their band gaps can be tuned by adjusting the metal halide framework and the organic species. They have high dielectric constant, high electron-hole diffusion lengths, high carrier mobility, high charge carrier lifetime, are polycrystalline, and show excellent ambivalent charge transport. The reason for the rapid rise in PCE of such devices is that perovskite materials have most of the properties required to be excellent absorbers; appropriate direct bandgap, high absorption coefficient, excellent carrier transport, and absence of deep trap states within the band gap leading to long carrier lifetime [44].

### 2.10.5 Transparent Conducting Oxide (TCO)

Fluorine doped tin oxide (FTO) is the most commonly used TCO for perovskite solar cells. ITO is also commonly used but the high price of indium, its relatively low conductivity on flexible substrates and the low mechanical resistance creates the need for finding transparent electrodes [45]. These alternatives must have good conductivity, high transparency, and relatively low price. Some promising materials reported as transparent electrodes carbon nanotubes, graphene, and silver nanowires [45].

### **2.10.6 Substrate Materials**

Perovskite solar cells can be fabricated on flexible or rigid substrates. The substrate can also be transparent or opaque, and possess electrical properties or be non-conducting. The choice of substrate depends on a number of factors: solar cell architecture, type of electrode, solar cell manufacturing process, and the final requirement of the device. The main substrates used are glass, plastic, ceramic coated polymer and metal foil. Most plastic substrates cannot support very high temperatures. This limits the maximum processing temperature. An example of a plastic substrate is poly (ethylene terephthalate) (PET), with a comparatively low price and low average surface roughness but shows insufficient stability against moisture [45]. Successful long-time functioning can be achieved by using environmental barriers to protect water and oxygen. Metal foil substrates offer the advantage of high processing temperature capability, dimensional stability, and excellent barrier properties for oxygen and water [45]. Glass is transparent, scratches resistance and shows zero gas transmission but cannot yet be processed roll-to-roll. FTO coated glass serves as transparent and substrate [41]. Ceramic coated polymers for example, ITO coated poly (ethylene terephthalate) (PET) has been used as a substrate to produce a flexible perovskite solar cell [46]. ITO films deposited on polymer substrates show high electrical resistances. This is because the substrate can only be heated to a limited extent due to their weak thermal resistance of polymers[45]. Xiaoyan W. et al. 2015. demonstrated the titanium (Ti) metal foil in a solid-state, flexible solar cell based on titanium (Ti) foil/TiO<sub>2</sub> nanotubes (TNTs) with organic–inorganic halide perovskite absorber and transparent carbon nanotube electrode [47] and obtained a PCE of 8.31%.

### **2.10.7 Processing Techniques of Perovskite Solar Cells**

#### **2.10.7.1 Spin Coating**

Spin coating is a method used to deposit uniform thin films on flat substrates. The coating materials are mixed with a suitable solvent (ink) and the mixture is applied to the center of the chemically prepared substrate that is either spinning at a low rate or not spinning at all. The substrate is then made to rotate at a higher speed (> 600 rpm). This enables the centripetal force in combination with the surface tension to pull the liquid coating into an even covering. During this high spinning rate, the solvent evaporates and the coating material is left on the substrate in an even covering. During spin coating, drying and annealing of the solvent occur simultaneously.

Properties of the solvent and additives, annealing and processing temperatures and the environments, have a profound impact on the final film quality.

The common spin coating defects include pin holes and comet streaks. Pin holes and comet streaks can be caused by dust and large particles respectively on the substrate, and also by particles in the solvent. Hellmanex III is generally recommended for dust and particulate matter while acetone/IPA for removal of residues on substrates. Finally, a glass substrate is chemically coated by using NaOH solution in order to produce “-OH” terminations in the surface of the substrate which is excellent for most coating processes. The advantage of spin coating is the ability to quickly and easily produce very uniform films from a few nanometers to a few microns. The disadvantage is that most of the material is wasted as it is being flung off the sides.

Spin coating of the perovskite layer in perovskite solar can be done in one-step coating or a two-step coating process. **Figure 2.8** shows a One-step and two-step coating g procedures to deposit  $\text{CH}_3\text{NH}_3\text{PbI}_3$  perovskite. Dimethyl acetamide (DMA), dimethyl formamide (DMF),  $\gamma$ -butyrolactone (GBL) and isopropyl alcohol (IPA) can be used as solvents.

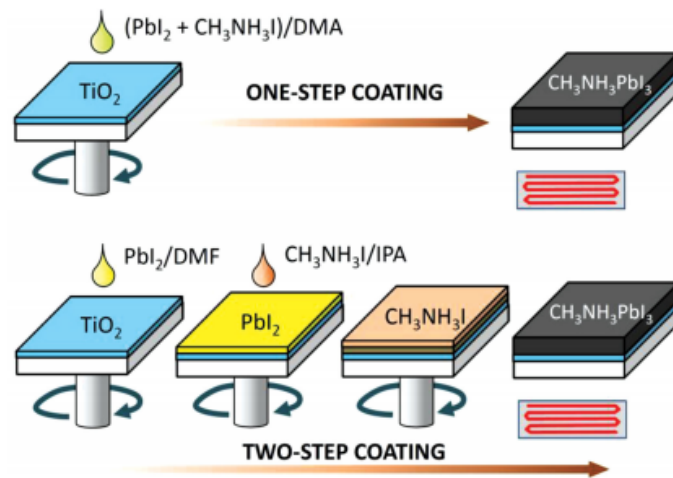


**Figure 2.8:** One-Step and Two-Step Coating Procedures to Deposit  $\text{CH}_3\text{NH}_3\text{PbI}_3$  Perovskite [48]

### 2.10.7.2 Thermal Evaporation

Thermal evaporation is a Physical Vapor Deposition (PVD) method for thin film deposition. It makes use of the vacuum technology to apply thin films of pure material(s) to the surface of a substrate. The crucible(s) containing the material(s) is (are) heated to a high temperature in a vacuum (pressure  $< 10^{-5}$  Torr) either by a filament or electron-beam (e-beam) methods. The material vaporizes and the vapor is transported to the target (substrate) at the top of the chamber. The film thickness is monitored precisely using a quartz balance. This is necessary as the deposition is not reproducible. Thermal vaporization can be a single source or dual-source. **Figure 2.9** shows a dual-source thermal evaporation system used for depositing perovskite. The organic source was  $\text{CH}_3\text{NH}_3\text{I}$  and the inorganic source  $\text{PbCl}_2$  for the deposition of  $\text{CH}_3\text{NH}_3\text{PbI}_{x-3}\text{Cl}_x$ , [42] whereas the deposition of  $\text{CH}_3\text{NH}_3\text{PbI}_3$ , the organic source was  $\text{CH}_3\text{NH}_3\text{I}$  and the inorganic source  $\text{PbI}_3$  [42]. Extremely uniform films were produced using this method.

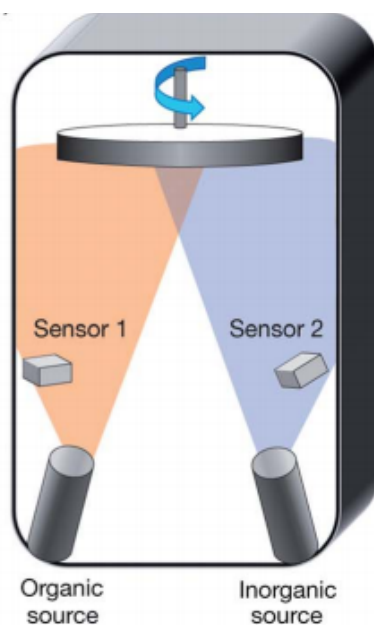


**Figure 2.9:** Dual-source thermal evaporation for deposition of perovskite absorber [42]

### 2.10.7.3 Vapor Assisted Solution Process (VASP)

In VASP for deposition of the perovskite layer, the inorganic film is first deposited by solution spin coating. This is followed by the deposition of the organic vapor on the pre-deposited

inorganic film by thermal evaporation method as shown in **Figure 2.10**. Chen et al developed the VASP by reacting MAI vapor and pre-deposited  $\text{PbI}_2$  to form  $\text{MAPbI}_3$  [44].

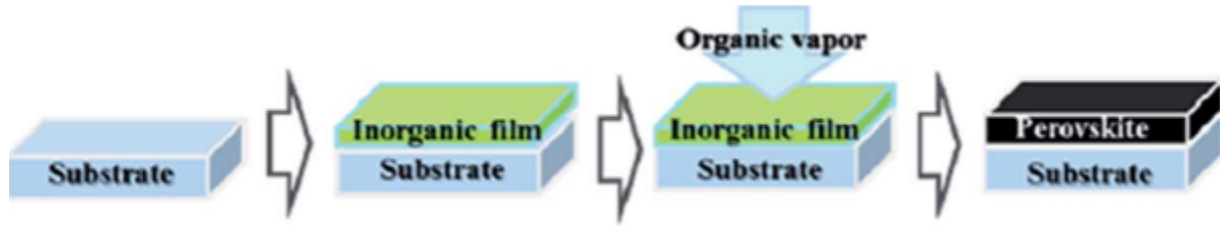


**Figure 2.10:** Vapor-assisted solution process using the MAI organic vapor to react with the  $\text{PbI}_2$  [44]

#### 2.10.7.4 Dip Coating

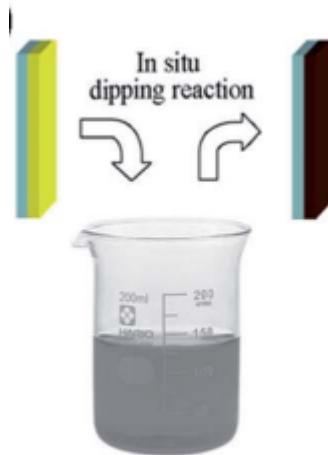


**Figure 2.11:** Sequential deposition by dipping the  $\text{PbI}_2$  in MAI Solution to form  $\text{MAPbI}_3$  [44]

#### 2.10.8 Physical Concepts of PSCs

PSCs have shown rapid progress in PCEs in the past five years because of some amazing intrinsic properties such as long range carrier diffusion lengths, am bipolar transport characteristic, high dielectric constant, low exciton binding energies, tunable bandgap and intrinsic ferroelectric polarization [49].

Long carrier diffusion lengths were demonstrated in solution processed polycrystalline  $\text{CH}_3\text{NH}_3\text{PbI}_3$  (~100 nm) and  $\text{CH}_3\text{NH}_3\text{PbI}_{3-x}\text{Cl}_x$  (~1  $\mu\text{m}$ ) [49]. Long diffusion length means that these materials can function effectively in thin film architecture, less energy loss by recombination and high collection of charge carriers at electrodes. The diffusion length ( $L_D$ ) is determined by the carrier lifetime ( $\tau$ ) and mobility ( $\mu$ ) according to the equation:

$$L_D = \sqrt{\frac{(K_B T \mu \tau)}{e}} \dots\dots\dots\text{Equation 2-6}$$

Where  $K_B$ ,  $T$  and  $e$ , are Boltzmann constant, absolute temperature and elementary charge respectively. The equation shows that the long diffusion length is due to long carrier lifetime and high carrier mobility. Long carrier lifetime is as a result of extremely low trap states within the bandgap of perovskite band structure [44]. The extremely low trap states also enable crystal growth with a much higher long range structural ordering and hence improving the carrier mobility greatly [33]. Recently, it has been reported that a greater fraction of the charges organic-inorganic halide perovskite is present as free electrons and holes, rather than bound excitons since the exciton binding energy is low enough to enable charge separation at room temperature [33][44].

**2.10.9 Principle of Light Absorption and Free Charge Generation**

It is well known that the perovskite layer in PSCs plays the role of a light absorber and bipolar carrier transport. As a light absorber, it absorbs part of the incident solar radiation, with photon energy greater than or equal to the energy band gap of any other semiconductor material. The absorption of photons results in the generation of electron-hole pairs that evolve toward the formation of highly delocalized Wannier excitons after thermalization [44]. A greater fraction of the excitons dissociates spontaneously back into free carriers [44]. The excitons and the free carriers coexist and their dynamic population continues to vary over their lifetime. The excitons diffuse to both sides of the perovskite layer where they meet the electron transport layer on one side and the HTL on the other side. The ETL attracts the free electrons and electrons from the excitons and the associated holes drift to the hole transport layer. The electrons attracted at the ETL are transported to the cathode. Also, the HTL attracts the free holes and holes from the excitons arriving there leaving electrons. The holes attracted by the HTL are transported to the anode. The electrons then drift to the ETL where they are attracted and transported to the

cathode. The ETL and HTL are therefore needed to assist in dissociating the excitons, separating and collecting electrons and holes.

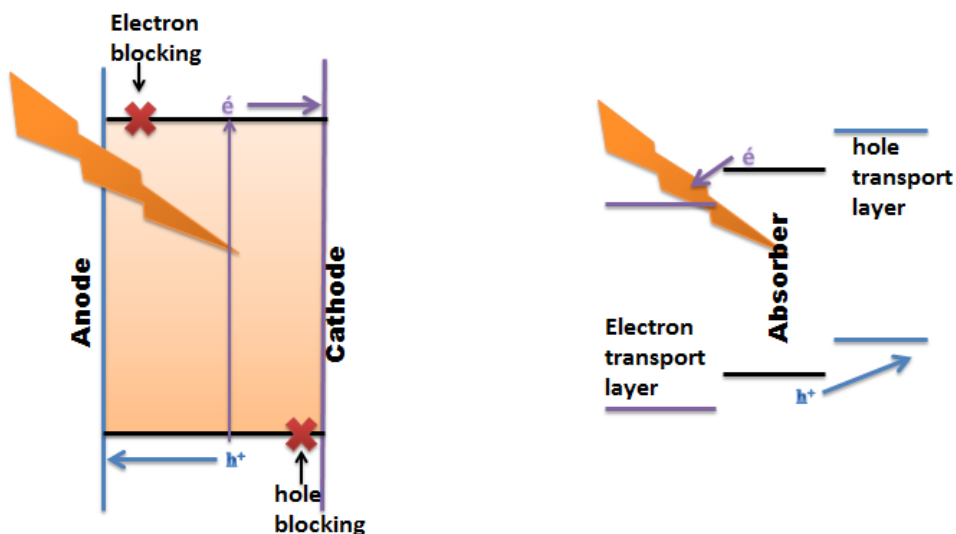


**Figure 2.12.** Free charge generation and transport

#### 2.10.10 Stability of PSCs

The degradation of most organic-inorganic perovskites is quite sensitive to water and moisture [50], for example,  $\text{CH}_3\text{NH}_3\text{PbI}_3$  degrades irreversibly when exposed to water and moisture. Thus, most of the fabrication process must be conducted in a glove box filled with inert gas. Jingbi You et al reported that the use of metal oxides as HTL and ETL instead of organic materials improves the stability of PSCs against water and oxygen [51]. In their report, the stability of a perovskite solar cell has  $\text{NiO}_x$  as HTL and  $\text{ZnO}$  as ETL was compared with that of PSCs containing organic transport layers. The metal oxide interface devices retained 90% of their efficiency after 60 days while the organic interface devices degraded completely after 5 days. It has also been reported that HTM-free cells exhibit excellent stabilities when used with thick back contacts such as carbon ( $10\ \mu\text{m}$ ) [52]. An airtight encapsulation could solve many related humidity problems of PSCs without modifying the efficient state-of-the art components but a decent encapsulation technology needs to be developed [52]. It has been shown that devices in which a mesoporous  $\text{TiO}_2$  layer is sensitized with the perovskite absorber are unstable to UV light [53]. The cause of the instability is associated with the interaction between the photo-generated holes inside the  $\text{TiO}_2$  and oxygen radicals on the surface of  $\text{TiO}_2$  [53].

### 2.10.11 Crystal Structure and Tolerance Factor of PSCs

A unit cell of organic-inorganic perovskite with formula  $ABX_3$  is composed of a cubic structure (alpha phase), where cation B (lead or tin) has six nearest-neighbors anions X (F, Cl, Br, I) and the cation A has twelve nearest-neighbors. The formability of perovskites is estimated based on its geometric tolerance factor,  $t$  [54],

$$t = \frac{(r_A + r_X)}{\sqrt{2}(r_B + r_X)} \dots\dots\dots \text{Equation 2-7}$$

Where  $r_A, r_B, r_X$ , are the effective ionic radii of A, B, and X respectively. In order to maintain the high cubic structure,  $t$ , should be close to 1 and could be between 0.813 and 1.107. Values of tolerance factor outside this usually result to non-perovskites.

**Table 2.2.** Ionic Radii for Some Ionic Species

S/N	IONIC SPECIES	IONIC RADIUS / Å
1	$F^-$	1.33
2	$Cl^-$	1.81
3	$Br^-$	1.96
4	$I^-$	2.20
5	$Sn^{+2}$	1.12
6	$Pb^{+2}$	1.19
7	$CH_3NH_3^+$	1.80

The tolerance factors for different perovskite materials are calculated using equation 2-7 and presented in the table below.

**Table 2.3.** Tolerance Factors for Organic-Inorganic Perovskites

S/N	PEROVSKITE	TOLERANCE FACTOR
1	$CH_3NH_3SnF_3$	0.90
2	$CH_3NH_3SnI_3$	0.85
3	$CH_3NH_3SnCl_3$	0.87
4	$CH_3NH_3SnBr_3$	0.86
5	$CH_3NH_3PbI_3$	0.83
6	$CH_3NH_3PbF_3$	0.89
7	$CH_3NH_3PbCl_3$	0.85
8	$CH_3NH_3PbBr_3$	0.84

## CHAPTER THREE

### EXPERIMENTAL PROCEDURE

#### 3.1 Equipment

The following equipment was used for this experimental work:

- Thermal Vacuum Evaporator
- Scanning Electron Microscope
- Keithley Source Meter
- UV/VIS Spectrophotometer
- Ultrasonic cleaner
- Hot plate
- Vacuum Oven
- Crucible
- Tweezers

#### 3.2 Chemicals

- Methyl ammonium tin iodide (Aldrich, 99.99%)
- Tin (II) iodide (Aldrich, 99.99%)
- Acetone
- Ethanol
- Deionized water.

#### 3.3 Fabrication of Perovskite Layer

The fabrication of the perovskite film was carried out in the following order: cleaning of glass slides; thermal vacuum evaporation of SnI<sub>2</sub> of the glass substrate; thermal vacuum evaporation of CH<sub>3</sub>NH<sub>3</sub>SnI<sub>3</sub> on SnI<sub>2</sub>/glass; post thermal annealing of the deposited perovskite film.

##### 3.3.1 Cleaning of Glass Slides

Prior to use, the glass slides are cleaned in an ultrasonic cleaner (VWR, Symphony) shown in **Figure 3.1** for 15 min in acetone at 30 °C, followed by 15 min in ethanol at 30 °C and finally in deionized (DI) water for 15 minutes at 30 °C. The cleaned glass slides were placed in a sample holder and allowed for at least a day to dry before being used for deposition.



**Figure 3.6.** Ultrasonic Cleaner

### 3.3.2 Sequential Thermal Vacuum Deposition of $\text{CH}_3\text{NH}_3\text{SnI}_3$

A 99.99 % tin (II) iodide powder was placed in the tungsten evaporating boat of the thermal vacuum evaporator (Nano 36, KURT J LESKER, MATENG D-A0040003, NORTH AMERICA) shown in **Figure 3.2**. A vacuum pump is used to achieve the vacuum in the chamber. The Z-factor for  $\text{SnI}_2$  was set at **1.1** and the density **7.3 g/cm<sup>3</sup>**. In order to find the optimum power that is required for evaporation of tin (II) iodide, several clever trials were performed. Good film coverage was obtained with the evaporator set as follows: ramp1, 5 % for 10 s, soak for 2 s, and ramp2, 10 % for 5 s and pressure  $1.9 \times 10^{-5}$  Torr. In order to establish the conditions for the deposition of methyl ammonium iodide, a 99.99 % methyl ammonium iodide was also placed in another tungsten boat (source 2) of the thermal evaporator and evaporated with the Z-factor set at **0.2** and density **2.2 g/cm<sup>3</sup>**. Several clever trials were performed. Good film coverage was obtained when the power rating was set as follows: ramp1, 3 % for 15 s, soak 0.0 s, and ramp2, 5 % for 5 s, pressure  $1.8 \times 10^{-5}$  Torr.



**Figure 3.7.** Nano 36 Thermal Vacuum Evaporator

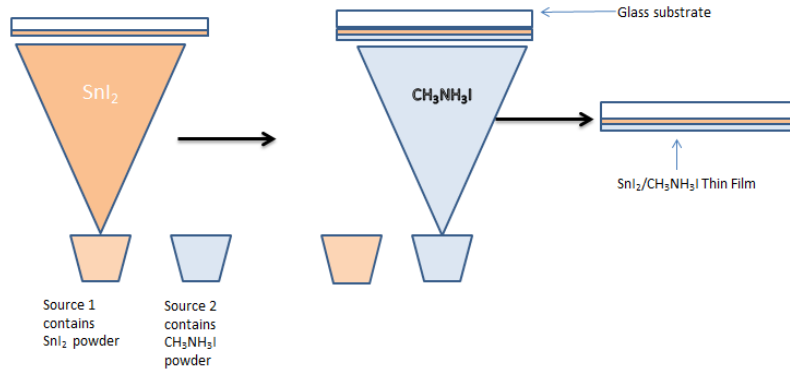


**Figure 3.8.** Sequential Thermal Evaporation of SnI<sub>2</sub>/CH<sub>3</sub>NH<sub>3</sub>I Thin Film

### 3.3.3 Annealing of CH<sub>3</sub>NH<sub>3</sub>SnI<sub>3</sub>

Annealing was done using a vacuum oven in a nitrogen environment. The annealing temperatures were 80 °C, 90 °C, 100 °C, 110 °C and 120 °C and annealing time 20 minutes. The reference sample was not annealed.

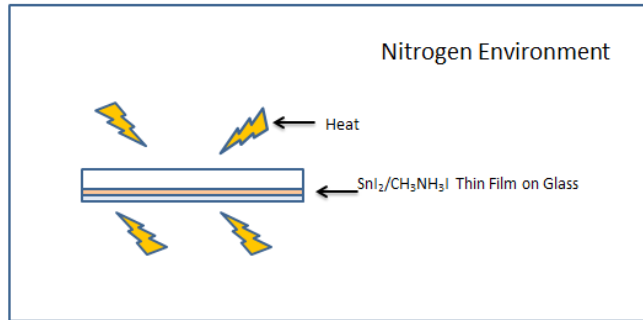


**Figure 3.9.** Annealing of SnI<sub>2</sub>/CH<sub>3</sub>NH<sub>3</sub>I in Vacuum Oven under Nitrogen Environment

## 3.4 Characterizations of CH<sub>3</sub>NH<sub>3</sub>SnI<sub>3</sub> Perovskite

### 3.4.1 Optical Measurement

The optical transmittance was measured using a UV/VIS AVASPEC 128 Fiber-Optic Spectrophotometer (Avantes BV, USA), **Figure 3.5**. Air was used as a reference in the measurement to ensure 100 % transmittance before mounting the sample. The sample was then gently placed on a sample holder between the light source and light detector before turning on the switch. The variation of optical transmittances of the annealed and un-annealed SnI<sub>2</sub>/CH<sub>3</sub>NH<sub>3</sub>I layer with time was measured.

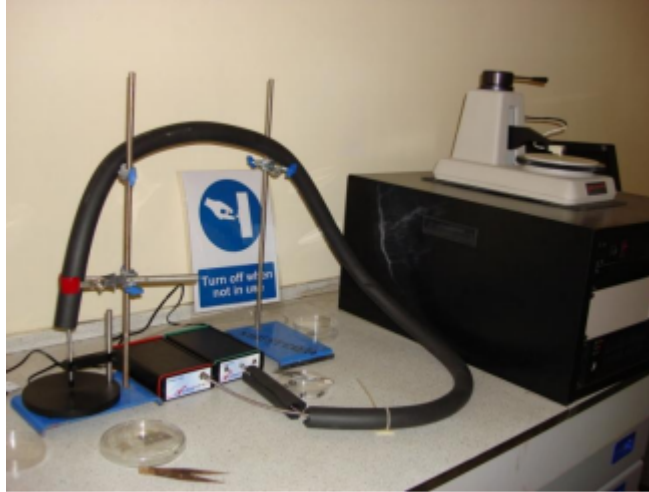


**Figure 3.10.** AVASPEC Fiber-Optic Spectrophotometer

### 3.5 Electrical Measurement

The sheet resistivity of the thin film was measured using the Keithley 2400 SMU ( Keithley Measurements, Cleveland, Ohio, USA) shown in **Figure 3.6**. The four point terminal of the device was used to probe the thin film during the measurement. The device was switched on and film thickness, previously measured with a surface profiler ( Veeco Instruments, Veeco Dektak 150), used as input. The resistivity was measured at four different positions on the film and the average value calculated.



**Figure 3.11.** Keithley Source Meter Unit set Up (Left) and X-ray Diffractometer (right)

#### 3.5.1 X-ray Diffraction (XRD)

The phase composition was determined using a diffractometer (GBC Scientific Equipment, Braeside Vic 3195, and Australia) as shown in **Figure 3.6** (right). The experiment was carried

out at the Nanotechnology and Advanced Materials (CEN&AM), Akure, Ondo State-Nigeria. CEN&AM is established under the national agency for science and engineering infrastructure (NASENI). The  $\lambda$ : A 1.5418 Å radiation was used with Ni beta filter.

## CHAPTER FOUR

### RESULTS AND DISCUSSIONS

#### 4.1 Variation of Transmittance with Annealing Temperature

**Figure 4.1** shows how the transmittance of  $\text{SnI}_2/\text{CH}_3\text{NH}_3\text{I}$  varies with annealing temperature. The films were annealed in a vacuum oven under a nitrogen atmosphere. The results show that the deposited  $\text{SnI}_2/\text{CH}_3\text{NH}_3\text{I}$  samples become more transparent when annealed in a nitrogen atmosphere and the transparency increases with an increase in annealing temperature. This may imply that annealing results in the formation of a product and the rate of formation is temperature dependent.

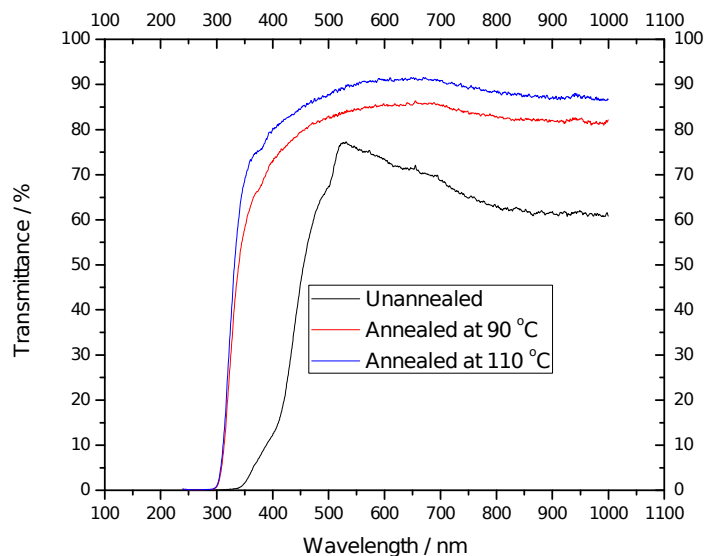


**Figure 4.12.** Variation of Transmittance of  $\text{SnI}_2/\text{CH}_3\text{NH}_3\text{I}$  with Annealing Temperature

#### 4.2 Stability of Un-Annealed and Annealed Films in Air

**Figure 4.2** shows how the transmittance of the as-deposited film changes when exposed to air. The result shows that the transparency of the un-annealed  $\text{SnI}_2/\text{CH}_3\text{NH}_3\text{I}$  increases in the air. This implies that the film is unstable as it may be reacting with the atmosphere to form a new product.

According to **Figure 4.3**, we see that after annealing, the transmittance is almost stable. This may imply a new product is formed during annealing and the product is more stable in air.

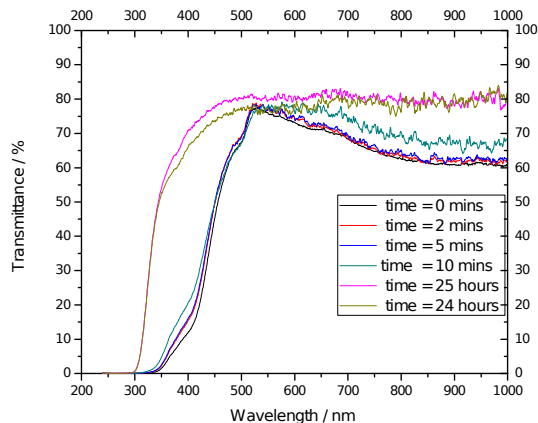


**Figure 4.13.** Variation of Transmittance of un-annealed  $\text{SnI}_2/\text{CH}_3\text{NH}_3\text{I}$  with time

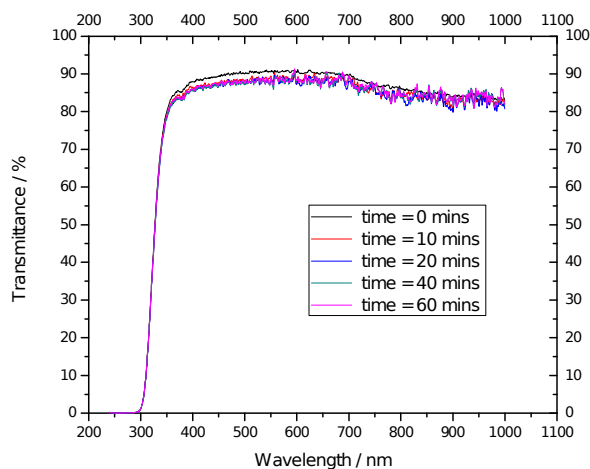


**Figure 4.14.** Variation of Transmittance of  $\text{SnI}_2/\text{CH}_3\text{NH}_3\text{I}$  Thin Film Annealed at  $110^\circ\text{C}$  with time

### 4.3 Absorption Coefficient, $\alpha$

**Figure 4.4** shows that the absorption coefficient depends on the annealing temperature. Since absorption coefficient is a material property, this may imply that different materials are formed during annealing. It is calculated from the intensity of the incident light ( $I_0$ ), the transmitted light ( $I$ ) and film thickness ( $d$ ). The transmitted intensity  $I$  is obtained from the experimental data used to plot equation 4-1. The film thicknesses  $d$  for used for calculating different values of  $\alpha$  are

given in **Table 4.1**. This is achieved by using equation 4-2 obtained from Beer Lambert's equation (equation 4-1).

$$I = I_o \exp(-\alpha d) \dots\dots\dots \text{Equation 4-6}$$

$$\alpha = \left(\frac{1}{d}\right) \left(\ln\left(\frac{I_o}{I}\right)\right) \dots\dots\dots \text{Equation 4-7}$$

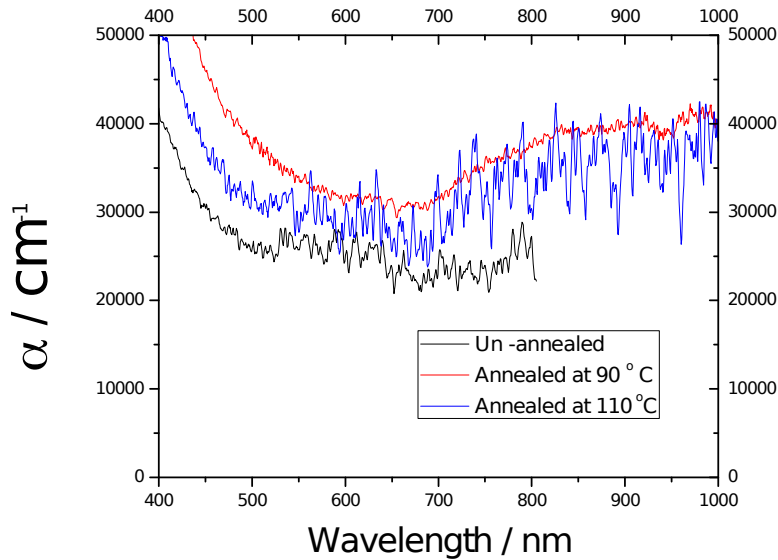


**Figure 4.15.** Variation of Absorption Coefficient of SnI<sub>2</sub>/CH<sub>3</sub>NH<sub>3</sub>I Thin Film with Annealing Temperature

The results show that the un-annealed film has the least absorption coefficient. The absorption coefficient when the film is annealed at 90 °C is greater than absorption coefficient when annealed at 110 °C and when un-annealed. Lead hybrid perovskite solar cells have absorption coefficients up to 1.5 x 10<sup>4</sup> cm<sup>-1</sup> at 550 nm [43]. The absorption coefficient obtained is about 3.0 x 10<sup>4</sup> cm<sup>-1</sup> at 550 nm. This result is comparable with that for lead hybrid perovskite PV.

**4.4 Variation Surface Roughness with Annealing Temperature**

**Figure 4.5** shows Scanning Probe Microscopy (SPM) images of the surfaces un-annealed film (a) and films annealed at 80 °C (b), 100 °C (c) and 120 °C (d). This was done using a nanoindenter (Hysitron TI 950 Triboindenter, Minneapolis, MN 55344, United States). **Figure 4.5** and **Table 4.1** show that the average roughness depends on annealing temperature. The

dependence is non-linear. Considering the possible errors in the measurement of the average surface roughness, **Table 4.1**, we see that the roughness of un-annealed sample is almost equal to the roughness of sample annealed at 80 °C but reduces for samples annealed at 100 °C and 120 °C. The change in surface roughness with temperature indicates that a temperature dependent transformation such as diffusion is taking place during annealing. This transformation results in the formation of materials with different surface morphologies.

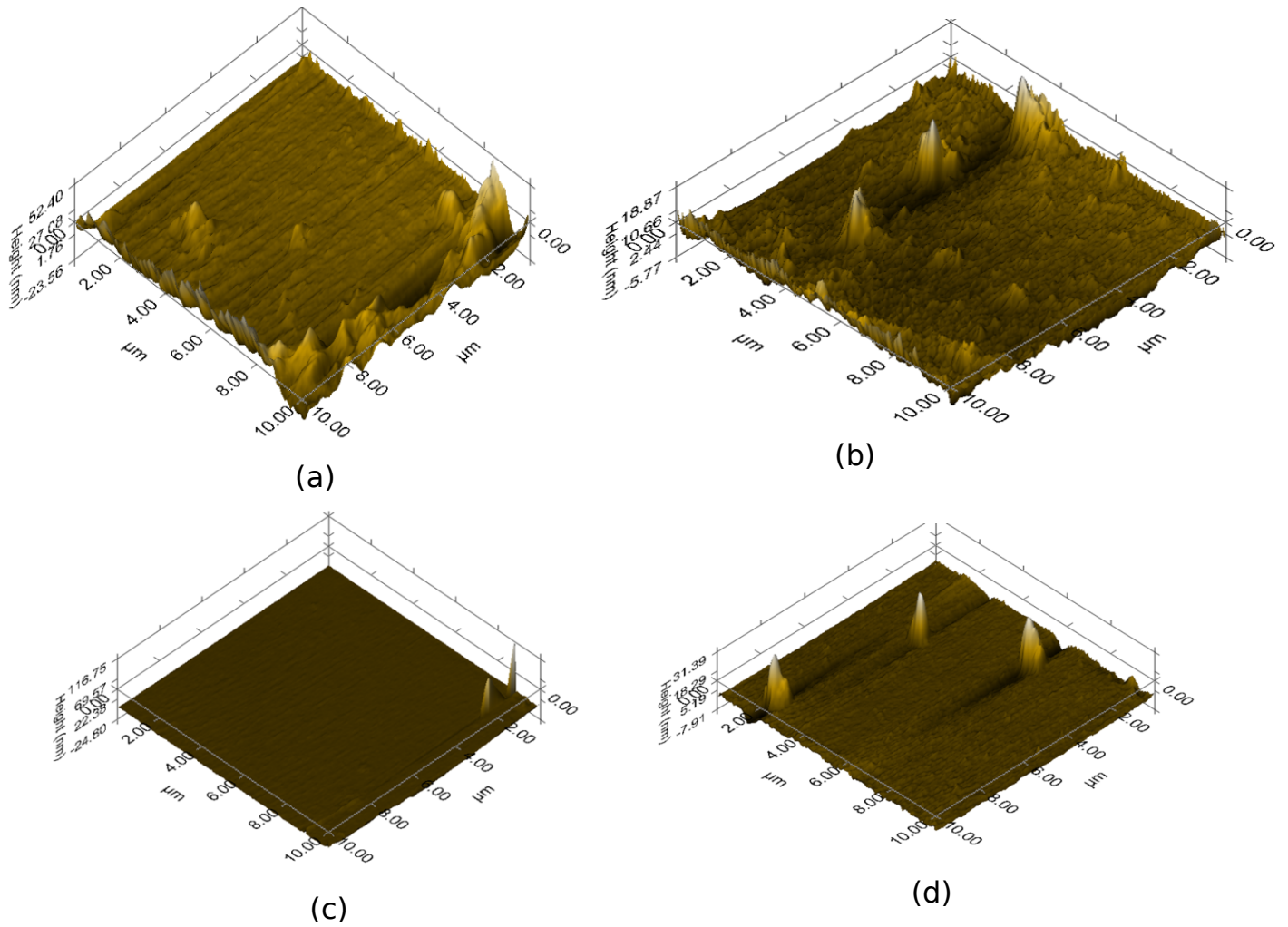


**Figure 4.16.** SPM Images of Surface Layer of Films Annealed at (b) 80 °C (c) 100 °C (d) 120 °C and (a) Un-annealed

**Table 4.4.** Roughness of SnI<sub>2</sub>/CH<sub>3</sub>NH<sub>3</sub>I Thin Films Annealed at Different Temperatures

Samples	Average surface roughness / Nm	Error on surface Roughness in nm $\pm$ 5 %	Thickness d / nm	Error on thickness d in nm $\pm$ 5 %
Un-annealed, Figure 4.5 (a)	0.9003	0.04501	100	5
Annealed at 80 °C, Figure 4.5 (b)	0.9752	0.04876	30	1.5
Annealed at 100 °C, Figure 4.5 (c)	0.2917	0.01459	50	2.5
Annealed at 120 °C, Figure 4.5 (d)	0.5175	0.02587	40	2

#### 4.5 Resistivity

In **Figure 4.6**, A is un-annealed SnI<sub>2</sub>/CH<sub>3</sub>NH<sub>3</sub>I thin film (as-deposited film) and B, C, D, and E are annealed at 80 °C, 90 °C, 100 °C, and 110 °C respectively. The figure shows that the resistivity of the un-annealed is greater than that for films annealed between 80 °C and 110 °C. There is a decrease in resistivity with an increase in annealing temperature up to a temperature of about 90 °C after its starts increasing. The measured values are of the order of 10  $\Omega$  cm. Well known values of resistivity for lead-based organic-inorganic perovskites is of the order 10<sup>3</sup>  $\Omega$  cm [34]. This implies that tin-based perovskite films have better-conducting properties than lead-based perovskites. Films annealed at 120 °C were non-conducting. The result suggests that there is a chemical change taking place during annealing. The initial transformation results in the formation of materials which are semiconducting up to some particular annealing temperature. Beyond this temperature, the resistivity starts increasing. This could be as a result of the decomposition of the materials formed or the formation of materials which are non-conducting alongside the semiconducting materials. At 120 °C, the non-conductivity could be as a result of noncrystalline or nonconducting phases.

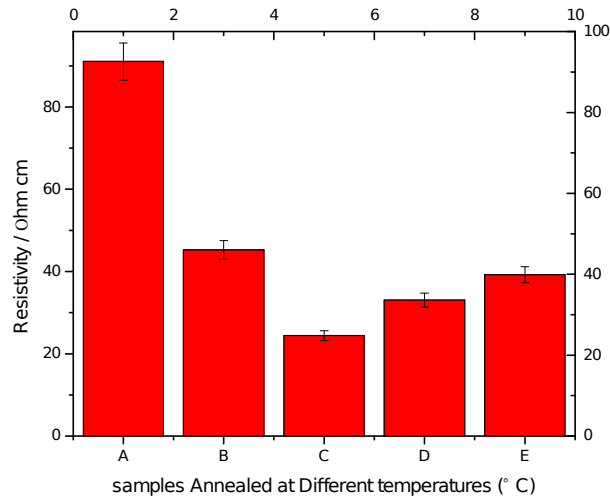


**Figure 4.17.** Variation of Resistivity with Post Annealing Temperature in Formation of SnI<sub>2</sub>/CH<sub>3</sub>NH<sub>3</sub>I Thin Film

#### 4.6 X-ray Diffraction (XRD)

**Figure 4.7** shows XRD result of un-annealed SnI<sub>2</sub>/CH<sub>3</sub>NH<sub>3</sub>I thin film while **Figure 4.8** shows the result of SnI<sub>2</sub>/CH<sub>3</sub>NH<sub>3</sub>I thin film that was annealed at 80 °C. Data corresponding to measurements of the Full-Width Half Maximum (FWHM) of the peaks observed in **Figure 4.6** was used to calculate the grain size by applying Scherrer's equation.

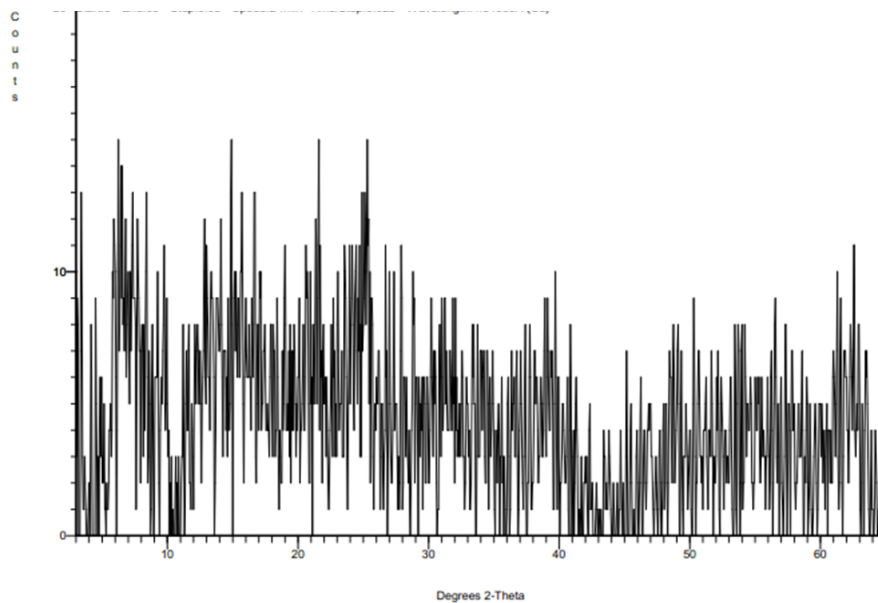


**Figure 4.7.** XRD for un-annealed Film

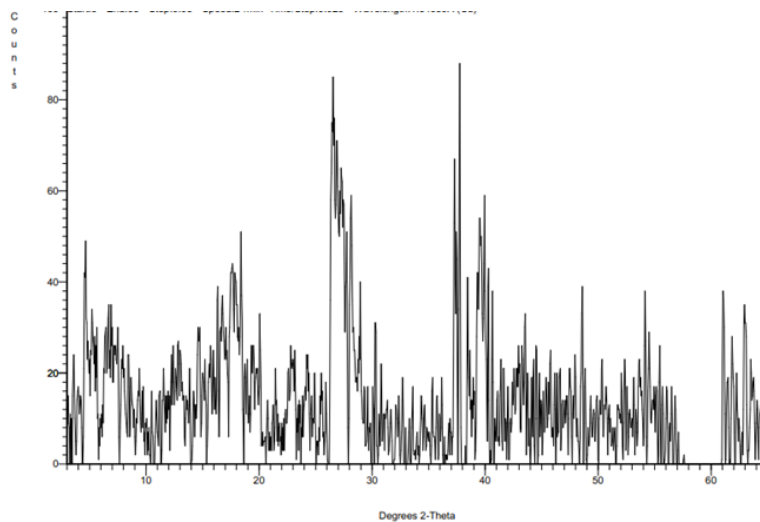


**Figure 4.8.** XRD for film annealed at 80 °C

The un-annealed  $\text{SnI}_2/\text{CH}_3\text{NH}_3\text{I}$  thin film (**Figure 4.7**) and films annealed at 120 °C (figure not shown) showed no peaks. This implies that all the components or phases present are amorphous. The un-annealed films correspond to a film of  $\text{CH}_3\text{NH}_3\text{I}$  on  $\text{SnI}_2$ . This may imply that  $\text{CH}_3\text{NH}_3\text{I}$  is amorphous or that a thin film of the amorphous layer is formed on  $\text{CH}_3\text{NH}_3\text{I}$  due to reaction with the atmosphere. The film annealed at 80 °C showed 39 peaks. This implies that some crystalline phases are formed at 80 °C. Peaks were seen at  $2\theta$  equals 39.5° at 80 °C. This is comparable with the results of  $\text{CH}_3\text{NH}_3\text{SnI}_3$  obtained by Noel et al. 2014 [2] (**Figure 4.9**). One

can, therefore, speculate that some of the peaks formed correspond to  $\text{CH}_3\text{NH}_3\text{SnI}_3$ . This implies that  $\text{CH}_3\text{NH}_3\text{SnI}_3$  may be formed when  $\text{SnI}_2/\text{CH}_3\text{NH}_3\text{I}$  is annealed at 80 °C and 100 °C. This is in line with results obtained by A. Dualeh et al. 2014 [55] and L.C.Chen et al. 2015 for Pb-based perovskites[56]. The calculated grain size at 80 °C is 6.620 nm. Small grains mean a large number of grain boundaries which act as scattering centers that impede the movement of electrons through the material.

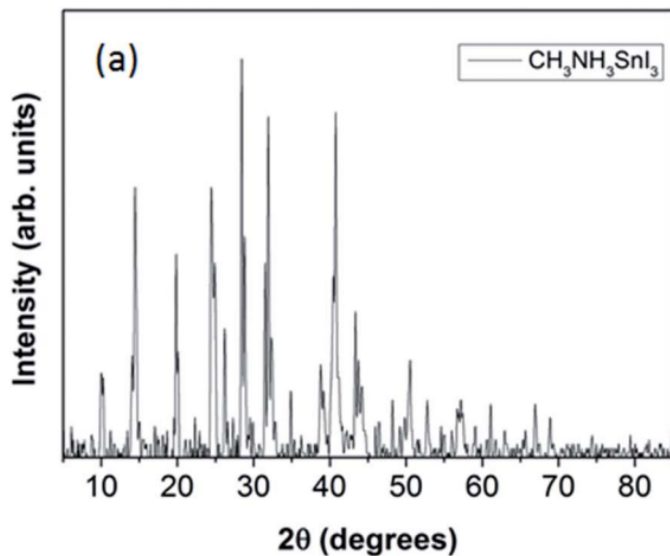


**Figure 4.9.** XRD Pattern Derived from Ground Powder of  $\text{CH}_3\text{NH}_3\text{SnI}_3$  [2]

## CHAPTER FIVE

### CONCLUSION AND RECOMMENDATIONS FOR FUTURE WORK

In this thesis,  $\text{SnI}_2/\text{CH}_3\text{NH}_3\text{I}$  was deposited and annealed. The conditions for thermal evaporation of  $\text{SnI}_2$  and  $\text{CH}_3\text{NH}_3\text{I}$  were established.  $\text{SnI}_2$  and  $\text{CH}_3\text{NH}_3\text{I}$  were deposited when the maximum ramp power of the Nano 36 thermal evaporator was 10 % and 5 % respectively.

The effect of post annealing temperature on the absorption coefficient, sheet resistivity, surface roughness, and composition was established. The greatest absorption and minimum resistivity were observed for annealing temperatures within the range 80 °C and 100 °C. The absorption coefficient was minimum when the film was un-annealed. Also, the sheet resistivity was higher for un-annealed films than for annealed films and at 120 °C, the film becomes non-conducting.

Measurements of sheet resistivity and absorption coefficient show that tin-based perovskites are better absorbers and conductors than lead-based perovskites.

We could speculate from XRD that un-annealed films and films annealed at 120 °C were amorphous while films annealed within 80 °C and 100 °C were crystalline. The crystallinity reduced as the temperature increased from 80 °C to 100 °C. Analysis of the results showed the presence of peaks which may correspond to  $\text{CH}_3\text{NH}_3\text{SnI}_3$ .

We may, therefore, conclude that post annealing is necessary for the formation of the  $\text{CH}_3\text{NH}_3\text{SnI}_3$  thin film and the best post annealing temperature range for the formation is between 80 °C to 100 °C, which is similar to the results obtained by A. Dualeh et al. in 2014 [55] for lead-based perovskite solar cells. This implies that tin-based perovskites are formed within the same temperature range like lead-based perovskites.

For future work, the optimum temperature and annealing time for the formation of tin-based perovskites need to be investigated. XRD measurements must be repeated for better optimization.

## REFERENCES

- [1] T. C. Sum and N. Mathews, “Advancements in Perovskite Solar Cells: Photophysics behind the Photovoltaics,” *Energy Environ. Sci.*, pp. 2518–2534, 2014.
- [2] N. K. Noel, S. D. Stranks, A. Abate, C. Wehrenfennig, S. Guarnera, A.-A. Haghighirad, A. Sadhanala, G. E. Eperon, S. K. Pathak, M. B. Johnston, A. Petrozza, L. M. Herz, and H. J. Snaith, “Lead-Free Organic-Inorganic Tin Halide Perovskites for Photovoltaic Applications,” *Energy Environ. Sci.*, vol. 7, pp. 3061–3068, 2014.
- [3] S. Chu and A. Majumdar, “Opportunities and challenges for a sustainable energy future,” *Nature*, vol. 488, no. 7411, pp. 294–303, Aug. 2012.
- [4] M. McGehee, “Emerging High-Efficiency Low-Cost Solar Cell Technologies.”
- [5] A. Kojima, K. Teshima, Y. Shirai, and T. Miyasaka, “Organometal Halide Perovskites as Visible-Light Sensitizers for Photovoltaic Cells,” *J. Am. Chem. Soc.*, vol. 131, no. 17, pp. 6050–6051, May 2009.
- [6] A. R. bin M. Yusoff and M. K. Nazeeruddin, “Organohalide Lead Perovskites for Photovoltaic Applications,” *J. Phys. Chem. Lett.*, vol. 7, no. 5, pp. 851–866, Mar. 2016.
- [7] P. Wang, Y. Guo, S. Yuan, C. Yan, J. Lin, Z. Liu, Y. Lu, C. Bai, Q. Lu, S. Dai, and C. Cai, “Advances in the structure and materials of perovskite solar cells,” *Res. Chem. Intermed.*, vol. 42, no. 2, pp. 625–639, Feb. 2016.
- [8] “How much energy does the Sun produce in one hour?” [Online]. Available: <http://www.astronomycafe.net/qadir/q1835.html>. [Accessed: 06-May-2016].
- [9] “Part 2: Solar Energy Reaching The Earth’s Surface.” [Online]. Available: <http://www.itacanet.org/the-sun-as-a-source-of-energy/part-2-solar-energy-reaching-the-earths-surface/>. [Accessed: 06-May-2016].
- [10] C. Piermarocchi, “Introduction to excitons and their role in photovoltaic processes.” Michigan State University, East Lansing, Michigan, 2008.
- [11] M. Tawheed Kibria, A. Ahammed, and S. Mahmud Sony, “A Review: Comparative studies

- on different generation solar cells technology,” 2014.
- [12] Fraunhofer Institute for Solar Energy and I. Systems, “PHOTOVOLTAICS REPORT.” 2016.
- [13] K. Jasim, “Dye sensitised solar cells—working principles, challenges and opportunities,” *A chapter Sol. Cells/b.*, 2011.
- [14] C. Nielsen, S. Holliday, and H. Chen, “Non-Fullerene Electron Acceptors for Use in Organic Solar Cells,” *Accounts Chem.*, 2015.
- [15] S. Berkley, “The Fabrication and Characterization of Organic Solar Cells,” 2009.
- [16] Brittany L. Oliva-ChatelainAndrew R. Barron, “An Introduction to Solar Cell Technology,” 2016. [Online]. Available: <https://cnx.org/contents/3QU3ovtd@1/An-Introduction-to-Solar-Cell->. [Accessed: 04-May-2016].
- [17] D. Derkacs and R. Jones-Albertus, “Multijunction solar cells,” *US Pat. App. 14/ ...*, 2013.
- [18] Christiana Honsberg and and Stuart Bowden, “A collection of resources for the photovoltaic educator.” [Online]. Available: <http://www.pveducation.org/pvcdrom/solar-cell-operation>. [Accessed: 07-May-2016].
- [19] A. Kojima, K. Teshima, Y. Shirai, and T. Miyasaka, “Organometal halide perovskites as visible-light sensitizers for photovoltaic cells,” *J. Am. Chem. Soc.*, vol. 131, no. 17, pp. 6050–1, May 2009.
- [20] J. Im, C. Lee, J. Lee, S. Park, and N. Park, “6.5% efficient perovskite quantum-dot-sensitized solar cell,” *Nanoscale*, 2011.
- [21] “Lead iodide perovskite sensitized all-solid-state submicron thin film mesoscopic solar cell with efficiency exceeding 9%,” *Sci. Rep.*, 2012.
- [22] J. Ball, M. Lee, A. Hey, and H. Snaith, “Low-temperature processed meso-superstructured to thin-film perovskite solar cells,” *Energy Environ. Sci.*, 2013.
- [23] “MAPbI<sub>3</sub>-xCl<sub>x</sub> Mixed Halide Perovskite for Hybrid Solar Cells: The Role of Chloride as

- Dopant on the Transport and Structural Properties,” *Chem.*, 2013.
- [24] H. Li, K. Cao, J. Cui, S. Liu, X. Qiao, Y. Shen, and M. Wang, “14.7% efficient mesoscopic perovskite solar cells using single walled carbon nanotubes/carbon composite counter electrodes,” *Nanoscale*, 2016.
- [25] “Low-temperature-processed ZnO–SnO<sub>2</sub> nanocomposite for efficient planar perovskite solar cells,” *Energy Mater. Sol. ...*, 2016.
- [26] A. Dualeh, N. Tétreault, T. Moehl, P. Gao, M. K. Nazeeruddin, and M. Grätzel, “Effect of Annealing Temperature on Film Morphology of Organic-Inorganic Hybrid Perovskite Solid-State Solar Cells,” *Adv. Funct. Mater.*, vol. 24, no. 21, pp. 3250–3258, Jun. 2014.
- [27] L.-C. Chen, C.-C. Chen, J.-C. Chen, and C.-G. Wu, “Annealing effects on high-performance CH<sub>3</sub>NH<sub>3</sub>PbI<sub>3</sub> perovskite solar cells prepared by solution-process,” *Sol. Energy*, vol. 122, pp. 1047–1051, 2015.
- [28] F. Hao, C. Stoumpos, D. Cao, and R. Chang, “Lead-free solid-state organic-inorganic halide perovskite solar cells,” *Nature*, 2014.
- [29] M. Kumar, S. Dharani, W. Leong, and P. Boix, “Lead-Free Halide Perovskite Solar Cells with High Photocurrents Realized Through Vacancy Modulation,” *Advanced*, 2014.
- [30] K. Marshall, R. Walton, and R. Hatton, “Tin perovskite/fullerene planar layer photovoltaics: improving the efficiency and stability of lead-free devices,” *J. Mater. Chem. A*, 2015.
- [31] J. Cui, H. Yuan, J. Li, X. Xu, Y. Shen, and H. Lin, “Recent progress in efficient hybrid lead halide perovskite solar cells,” *Technol. ...*, 2016.
- [32] K. Wojciechowski, M. Saliba, and T. Leijtens, “Sub-150 C processed meso-structured perovskite solar cells with enhanced efficiency,” *Environ. ...*, 2014.
- [33] “Excitons versus free charges in organo-lead tri-halide perovskites,” *Nature*, 2014.
- [34] J. Fan, B. Jia, and M. Gu, “Perovskite-based low-cost and high-efficiency hybrid halide solar cells,” *Photonics Res.*, 2014.

- [35] M. Ahmed, A. Habib, and S. Javaid, "Perovskite Solar Cells: Potentials, Challenges, and Opportunities," *Int. J.*, 2015.
- [36] Z. Hawash, L. Ono, S. Raga, and M. Lee, "Air-exposure induced dopant redistribution and energy level shifts in spin-coated spiro-MeOTAD films," *Chem.*, 2015.
- [37] Z. Hawash, L. Ono, S. Raga, and M. Lee, "Air-exposure induced dopant redistribution and energy level shifts in spin-coated spiro-MeOTAD films," *Chem.*, 2015.
- [38] P. Qin, S. Tanaka, S. Ito, N. Tetreault, and K. Manabe, "Inorganic hole conductor-based lead halide perovskite solar cells with 12.4% conversion efficiency," *Nature*, 2014.
- [39] S. Gupta and A. Gupta, "Mathematical formulation comparative analysis of losses in solar cells," *tutorialspoint.com*.
- [40] M. Li, P. Shen, K. Wang, T. Guo, and P. Chen, "Correction: Inorganic p-type contact materials for perovskite-based solar cells," *J. Mater. Chem. A*, 2015.
- [41] J. Ball, M. Lee, A. Hey, and H. Snaith, "Low-temperature processed meso-superstructured to thin-film perovskite solar cells," *Energy Environ. Sci.*, 2013.
- [42] T. Sum and N. Mathews, "Advancements in perovskite solar cells: photophysics behind the photovoltaics," *Energy Environ. Sci.*, 2014.
- [43] J. Cui, H. Yuan, J. Li, X. Xu, and Y. Shen, "Recent progress in efficient hybrid lead halide perovskite solar cells," *Sci. Technol. Adv. Mater.*, vol. 16, no. 3, p. 36004.
- [44] T. Song, Q. Chen, H. Zhou, C. Jiang, and H. Wang, "Perovskite solar cells: film formation and properties," *J. Mater.*, 2015.
- [45] B. Rand and H. Richter, *Organic Solar Cells: fundamentals, devices, and upscaling*. 2014.
- [46] P. Docampo, J. Ball, M. Darwich, and G. Eperon, "Efficient organometal trihalide perovskite planar-heterojunction solar cells on flexible polymer substrates," *Nature*, 2013.
- [47] X. Wang, Z. Li, W. Xu, S. Kulkarni, S. Batabyal, and S. Zhang, "TiO<sub>2</sub> nanotube arrays based flexible perovskite solar cells with transparent carbon nanotube electrode," *Nano*

*Energy*, 2015.

- [48] H. S. Jung and N. G. Park, “Perovskite solar cells: From materials to devices,” *Small*, vol. 11, no. 1, pp. 10–25, 2015.
- [49] Y. Hsiao, T. Wu, M. Li, Q. Liu, W. Qin, and B. Hu, “Fundamental physics behind high-efficiency organo-metal halide perovskite solar cells,” *J. Mater.*, 2015.
- [50] G. Niu, X. Guo, and L. Wang, “Review of recent progress in chemical stability of perovskite solar cells,” *J. Mater. Chem. A*, 2015.
- [51] “Improved air stability of perovskite solar cells via solution-processed metal oxide transport layers,” *Nature*, 2016.
- [52] S. Emami, L. Andrade, and A. Mendes, “Recent progress in long-term stability of perovskite solar cells,” *Porto J. Eng.*, 2015.
- [53] T. Leijtens, G. Eperon, S. Pathak, and A. Abate, “Overcoming ultraviolet light instability of sensitized TiO<sub>2</sub> with meso-superstructured organometal tri-halide perovskite solar cells,” *Nature*, 2013.
- [54] Y. Zhao and K. Zhu, “Organic–inorganic hybrid lead halide perovskites for optoelectronic and electronic applications,” *Chem. Soc. Rev.*, 2016.
- [55] A. Dualeh, N. Tregreault, T. Moehl, P. Gao, M. K. Nazeeruddin, and M. Grätzel, “Effect of annealing temperature on film morphology of organic-inorganic hybrid perovskite solid-state solar cells,” *Adv. Funct. Mater.*, vol. 24, no. 21, pp. 3250–3258, 2014.
- [56] L. C. Chen, C. C. Chen, J. C. Chen, and C. G. Wu, “Annealing effects on high-performance CH<sub>3</sub>NH<sub>3</sub>PbI<sub>3</sub> perovskite solar cells prepared by solution-process,” *Sol. Energy*, vol. 122, pp. 1047–1051, 2015.